UNIVERSIDAD CARLOS III DE MADRID

Escuela Politécnica Superior

HIGH-EFFICIENCY SMA-BASED ACTUATOR

Jose Manuel Martín Pérez-Solórzano

supervised by
Luis Moreno

June 15, 2016

ABSTRACT

Design proposal and implementation analysis of an alternative high displacement flexible SMA-based actuator topology, targeting improved energy efficiency and actuation time, by completely overhauling SMA wire's surrounding conditions, specifically adding high heat capacity fluids and improving thermal management.

Contents

List of Figures

List of Tables

1 Introduction

1.1 Motivation

The increasing percentage of population in the over 65 years old bracket is a well researched topic due to its economic implications on developed countries, where birth rates have been stagnated or steadily decreasing for the last 40 years, in some countries even going below the replacement rate, while at the same time, life expectancy has kept increasing to about 85 years on these same countries [2].

The aspects driving the tendency of these two parameters are many, with key players being socio-economic status of large population groups and healthcare technological advances. Expecting no reversing trend on these aspects, the projections for growth of the mentioned bracket is then quite a reality.

The best way to portray this situation is through a population pyramid like the ones below. Figure 1 shows Europe projection by the European Parliamentary Research Service, which serves as a reference point for all developed countries. Figure 2 shows Japan's bleak future, setting the bar both as one of the most developed countries in the world and as one of the most population top-heavy pyramids.

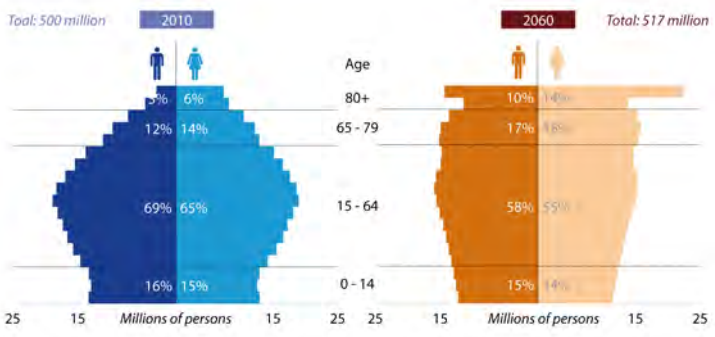

Figure 1: Ageing population: projections 2010 - 2060 for the EU27 [3]

The economic implications are huge, with such a large group of population in retirement benefitting from a pension, and an ever-thinning work force to pay debt. Even more dramatic is the fact that there won't be enough young people to take care of the older generations.

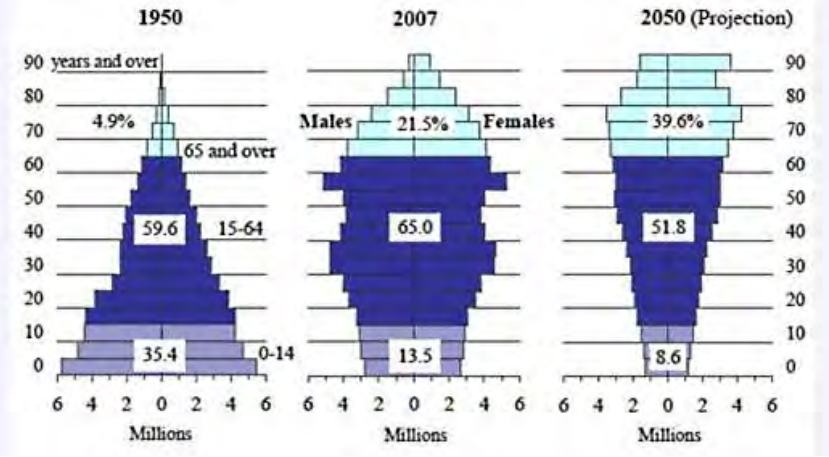

Figure 2: Japan's Population Pyramid Projection by Japan Statistics Bureau [4]

Related to this are **rehabilitation** needs for this growing population bracket, as well as any other individual, who an active rehabilitation method might benefit, due to faster and improved odds of rehabilitation. [5]

Proposed solutions take two relatable but diverging approaches. First are **robotic nurses** which intend to replace nurses and porters with robotic hardware and artificial intelligence, maintaining the current roles and capabilities of each of the agents involved. Then there are **exoskeletons**, an approach which acknowledges that an elder individual may be able to take care of himself or herself if he or she is able-bodied through the use of external hardware.

Both solutions present an incredible engineering feat that is yet to be solved reliably, and both will be needed in the long term. A fully-integrated fully-autonomous robot with porter's dexterity and strength, nurse's analytical knowledge and human-like interaction capabilities versus a supporting exoskeleton that doesn't alter or even improves the user's biomechanics while his or her intentions are flawlessly executed without hurting the wearer.

Technologywise, exoskeletons, our line of work, from a broad perspective require improved actuators regarding both power density, power-to-weight ratio, efficiency and price, as well as more reliable sensoring of user intentions.

1.2 Shape Memory Alloys

Shape memory alloys fall in the category of smart materials, being thermoelastic intermetallic alloys that show superelastic or shape memory behaviour at different temperatures.

First discovered by Arne Olande in 1938, when he observed the shape and recovery ability of a gold-cadmium alloy. W.J. Buehler and Wang at the US Naval Ordinance Laboratory in 1963 observed the shape memory effect in a nickel and titanium alloy, today known as nitinol ("Night in All Night in All"; Nickel Titanium Naval Ordinance Lab) while searching for materials that could be used in tools for dismantling magnetic mines.

In an article published by Time in 1968, discoverer William Buehler discussed how he thought nitinol might be used to prefabricate tools used in deep water or space. At the time, Goodyear Aerospace Corp. had envisioned deforming a nitinol satellite antenna and placing it into a small rocket payload, then restoring it to its original shape upon deployment by using heat.

SMAs change shape based on a solid-state phase transformation taking place at the atomic level. First they allow for some deformation percentage on their martensite phase, then, when heat is transferred to go from martensite to austenite phase, reducing euclidean three dimensional distance between corners of the lattice while exerting notable forces.

In their superelastic temperature range, polycrystalline alloys will undergo up to 8% deformation and recover their initial shape upon removal of the applied load. In the shape memory temperature range the alloys will recover up to 8% strain when heated through the recovery temperature range.

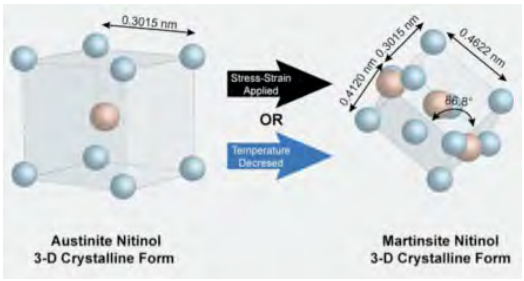

Figure 3: Austenite Martensite Phase Transformation

Nitinol parameters should be provided by the manufacturer as shape memory alloy behaviour is not standardized, although usually involving thermomechanical cycling with temperatures over 600 ° C. On Table 2 our particular wire parameters are listed. From Nickel's 8900 kg/m^3 density and Titanium's 4430 kg/m^3 one, percentage composition can be inferred, indicating close to a 1:1 ratio.

Table 1: Nitinol Parameters

Property	Nitinol	Unit
Density	6500	kg/m^3
Young Modulus	40 (M) / 75 (A)	GPa
Thermal Conductivity	18	$W/m \cdot K$
Thermal Expansion	6.6 (M) / 11 (A)	$10^{-6}/°C$
Melting Point	1310	C
Electrical Resistivity	76 (M) / 82 (A)	$\mu ohm \cdot cm$

Table 2: Wire Parameters

Property	SmartFlex05	Unit
Diameter	500	μm
A_s	60	C
Repetitive Elongation	4-5	%
Repetitive Force	33	N
Max. Force	118	N

Repetitive elongation and force exerted by the actuator are related to material fatigue, which is a thermomechanical process affected by load/tensile strength, temperature, time and number of cycles. The graph shown in Figure 4 gives some insight on some of those aspects. For an actuator devoted to an exoskeleton we definitely want to maximize the number of actuations.

Lastly, heat related parameters must be empirically tested. Both latent heat phase change and specific heat capacity can be measured using DSC, a technique which compares the heat required to increase the temperature of a sample, in our case a SMA wire, against a reference, plotting the heat flow as a function of temperature as shown in Figure 4. From variations in the heat flow curve, temperature phase transformation start and finish can be pinpointed. Given the thermomechanical dependence of some these variables they only serve as a reference, with highly complex models required to couple latent heat and mechanical opera-

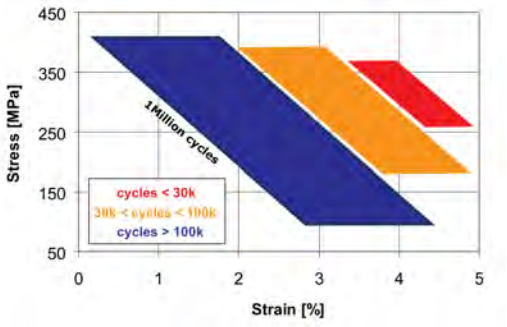

Figure 4: Stress-Strain Fatigue Trade-Off

tion [10].

From Figure 6 and 7 temperature phase change and temperature-force parameters on Table 3 are inferred.

Table 3: Heat Parameters

Property	SMA	Unit
Specific Heat Capacity	480	J/kg·K
Latent heat	24000	J/kg
Hysteresis Width	40-50	C
A_s @ 200 MPa	60	C
A_f @ 200 MPa	72	C
M_s @ 200 MPa	40	C
M_f @ 200 MPa	30	C
Temperature-Force	0.17	C/MPa

A certain length of SMA wire enters bulk phase transformation when it reaches austenite start temperature, A_s, and has almost 100% of its volume actuated or in contraction when austenite finish temperature, A_f is surpassed. The same can be said for martensite phase when temperature is decreasing, progressively entering relaxation, thanks to martensite's reduced Young modulus.

The actuated volume fraction as a function of material temperature during phase transformation ($A_s < T < A_f$) has been found [21] to fit the Roger-Liang equation:

$$\varepsilon = \frac{1}{2}\left[\cos\left(\pi \cdot \frac{T - A_s}{A_f - A_s}\right)\right] \tag{1}$$

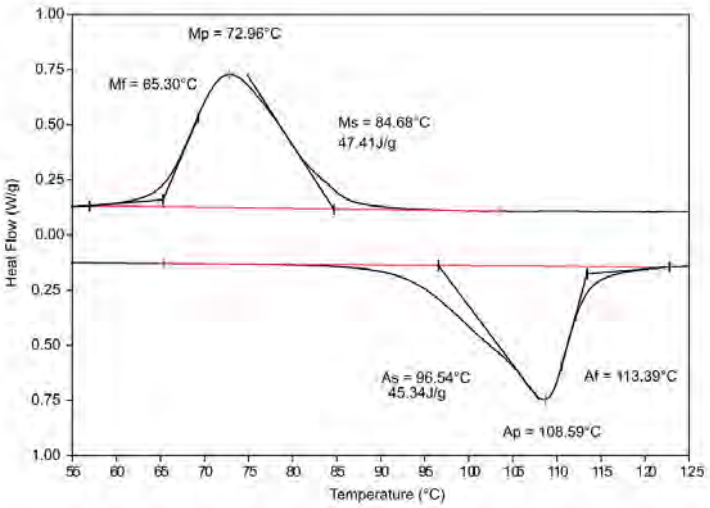

Figure 5: Shape Memory Alloy DSC

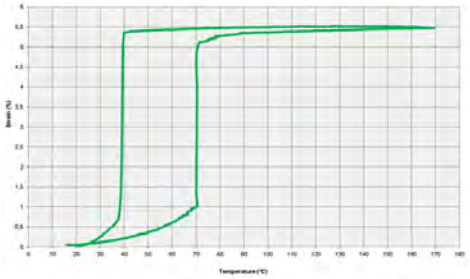

Figure 6: SmartFlex05 Strain-Temperature Curve. Courtesy of SAES Getters

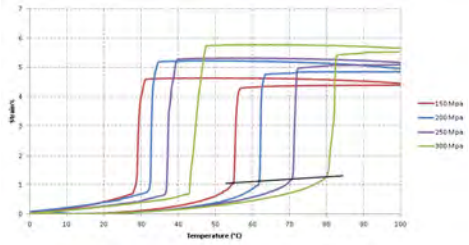

Figure 7: SmartFlex03 Transformation Temperature Change. Courtesy of SAES Getters

1.3 Simulation and Prototyping Software

Computer-Aide Simulation analysis for the present work has been performed using various suites.

Solid Edge - CAD Design and Linear Static FEM

Finite element analysis, FEA, subdivides a 3-dimensional problem into smaller, simpler, parts, called finite elements. The simplified equations that model these finite elements are then assembled into a larger system of equations that models the entire problem. FEA then uses differential to approximate a solution by minimizing an associated error function, so that it may represent as close as possible a real test setup.

Energy2D - 2D Heat Propagation Simulation [**?**]

Simplistic free CAD software that combines preprocessor, solver, and post-processor into a highly usable package. Provides an extremely accurate conduction simulator, while having a lackluster performance on convection and radiation.

Proteus 8 - electrical circuit testing and PCB routing

2 State of the Art

Robotic actuators pose specific requirements on power density, power-to-weight ratio, torque-to-weight ratio, movement range, controllability, efficiency of actuation, thermal design and other associated electromechanical aspects that the hardware designer must adhere to in order to obtain a reliable actuator for its application.

When these actuators are to be used in a supporting exoskeleton or an upper limb one, which is the target of this research, the same set of characteristics apply, but with even more stringent target figures, specially for upper limbs, having to provide the missing muscle strength while doing so in a less favourable actuating position compared to the human muscles .

With almost 60 years of technical development in the field of robotics, we can find actuators in many shapes and forms, each one with its pros and cons regarding its employability. The main solutions for this application that can be found deployed can be sorted as:

2.1 Electric Motors

Usually high on the efficiency scale, for both the actual motor and its controller, for general applications, their efficiency is notably affected by size and the range of speeds and loads required at the output, that also limits their heat dissipation capabilities. In this category brushless DC motors would be preferred for its responsiveness, quick acceleration, reliability, long life spans, high speed operation and a high power density.

Paired to the motor there will have to be some mechanical transmission converter that turns its high rotational speed an low torque, to a usable slower one that at the same time increases its torque, presenting a tough decision for the designer when aggresive control strategies that require both maximum speed and maximum torque are to be applied through the actuator.

The tandem will generally be completed by a gearbox, which in itself can be a major contributor to power loss and drop in efficiency, specially for high torque and small size due to manufacturing limitations. Theoretical limits on efficiency for sufficiently small motors and gears are as low as $0.66 \cdot 0.66 = 34\%$, with a real figure easily below 20% once variable load and controller are fed into the equation. Higher efficiency alternative on mechanical transmission might be belt pulleys, at the expense of added volume and weight, or an harmonic drive, with increased price.

The other drawback for electric motors is ironically its compactness and relative bulkiness, with its output shaft having to be next to the actuated joint, so that even though the power-to-weight ratio figures are good, each actuator in a joint chain has to carry the weight of all the motors below it. This may be avoided by mechanical transmission using wires passing through ball bearings on angles or using Bowden cable principle, or through pneumatic/hydraulic transmission lines, at the sacrifice of greatly increased actuator design and assembly complexity, but definitely one of the most interesting options.

Figure 8: HAL Upper Limb Exoskeleton

Relevant implementations for upper limb exoskeletons that include electric motors are CSIC's WOTAS, devoted to rehabilitation research [11], University of Pennsylvania's Titan Arm, a lowcost solution which exploits bowden cable mechanical transmission link to lift up to 18 kg [12], and Cyberdyne's HAL, commercial product that sets the current benchmark for performance of such portable actuator, actuating 120 degrees, weighting in at 1.5 kg and allowing for 120 minutes of nominal operation [13].

2.2 Alternative Actuators

Pneumatic and hydraulic linear actuators probably are the ones most reliably used for humanoid applications, usually the latter taking the upper hand in most aspects [14]. Even though different technologies, operation is based around a piston inside a hollow cylinder that is moved through pressure differential between faces. This requires the use of an external pump, automatic or manual, that affects its power-to-weight ratio as well as its user-friendliness due to the loudness in operation.

Pneumatic offers lightweight and low price over other linear actuators, but due to pressure losses and air's compressibility they are less efficient, and reducing operating pressure means lower specific power. A compressor must run continually even if nothing is moving, or they can opt to use a compressed air container and have a limited operating time. Also its precise controllability requires proportional regulators and valves, raising costs and complexity. For our application efficiency would be easily flying below 15

Exploiting air's compressibility, there are now lines of work in soft robotics that achieve compliance making use of pneumatic transmission lines and rolling-diaphragm cylinders [15] or soft/inflatable containers, either just longitudinally, as in pneumatic muscles, or in multiple degrees of freedom as shown by OtherLab Orthodics, using a compound inflatable structure as seen in Figure 9.

Figure 9: Compound Inflatable Structure Exosuit

On the other hand, hydraulic actuators can have up to 25 times the power density of pneumatic actuators and easily double the power-to-weight ratio, hence their use on power intensive tasks. They are also able to maintain position without having to provide additional energy. Unluckily, it has its own set of disadvantages, with leaked fluid being one of them due to high pressures, that reduces efficiency and reliability, another being the efficiency loss with size constraints, being even more affected that electric motors and finally its power density reduction, as apart from the mentioned pump, these actuators require many other companion parts, including a fluid reservoir, motors, release valves and heat exchangers, along with noise-reduction equipment that target the key mobile-application requirement of power-to-weight ratio.

Figure 10: Boston Dynamics' Atlas 2016 Leg Detail

Although Boston Dynamics has not been actively involved in exoskeletons yet, expecting to do so soon [17], their work extending on MIT's Leg Laboratory for robotic humanoids has to be mentioned, making the most reliable use seen until now of hydraulic actuators, most recently on its Atlas 2016 update, showcasing what embedded design at all levels can bring to the table, where supporting structure is used for fluid piping, and so being an inspiration for this project [18].

2.3 SMA Actuators

The field of exoskeletons has seen many technologies being deployed searching for higher reliability. SMAs are a relatively new candidate in this field due to its exoticness and intrinsic low energy efficiency, but they compensate excelling on both their power density and power-to-weight ratio, that can be easily adapted to torque-to-weight ratio.

Current Robotics Lab SMA-based actuators make use of relatively long nitinol wires housed in Bowden cables for mechanical force transmission, which allow them to remain conformable to the shape of a human body, so that they can be concealed around the wearer's body.

Wire length provides sufficient linear actuation, obtained from its repetitive elongation percentage, while wire cross section and number of wires are adjusted to the actuator's force requirements. To control the wire's length its temperature is balanced using Joule effect and metal to air dissipation, which in turn results in a percentage of wire being in austenite, or in contraction, while the rest is in martensite, or in relaxation, along its longitudinal length.

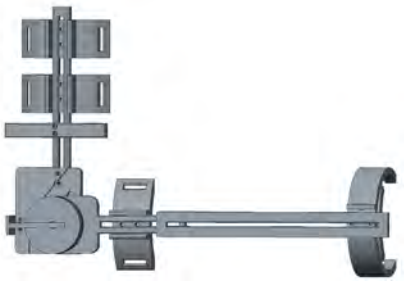

Figure 11: 2 DoF Upper Limb Exoskeleton

As showcased on previous research [19], controllability of position and speed has been solved closing the feedback loop by sensing longitudinal displacement at the loaded end of the SMA wire with a hall effect sensor.

Moving into application, there are two upper limb exoskeleton topologies in development. Their purpose is elbow rehabilitation, working tightly with physicians on its development. Forearm mass represents around 1.5% of body weight [20], about 1.20 kg for an adult, 0.75 kg for a child, anatomical centre of mass has its loci about 43% of forearm total length from the elbow, and transversal moment of inertia is around $0.005 \mathrm{kg} \cdot \mathrm{m}^2$.

First one, and furthest developed, makes use of a polyamide 3D printed stiff 2 DoF setup, on Figure 11, for elbow joint support actuated by 3 SMA wires providing 120 ° of actuation. Its setup has also been a development platform for improved mechanical design and control strategies, with some knowledge pertaining to this present project already being poured into that development.

Second one dives deeper into experimental grounds, on Figure 12, running along the wearer's arm, keeping the amount of external elements to a minimum by exploiting the underlying bone structure. The potential is huge, but the number of unknowns goes up as the setup relies more on external mechanical support.

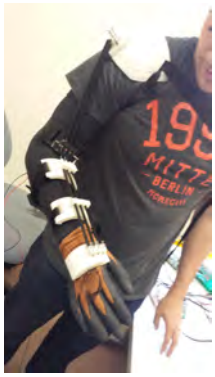

Figure 12: Experimental Exoskeleton

The main handicap on working SMA-based actuators is its intrinsic low-efficiency, that is brought further down by having continuous heat dissipation towards the surrounding metallic Bowden tubing sheath while heating or maintaining position, that cannot be restricted, as SMA wire cooling relies on this heat flow to lower wire's temperature, resulting also in an asymmetric time response between heating and cooling cycles, inherent to natural air convection from Bowden tubing reduced convective coefficient versus Joule effect's high internal heat generation.

3 Objectives

The main objetive for this bachelor's thesis is then to design a SMA-based actuator that retains the main advantages of the previous actuators and improves on the actuation cycle time and its efficiency, achieving this by adding fluids and thermal isolation into the equation.

Having to develop an actuator from scratch various testing setups will be used for empirical evaluation of the theoretical propositions, with imposed constraints that allow for specific parameter testing.

For these tests, our setups will revolve around a single SmartFlex05 500 μm nitinol wire of 0.5m that will actuate a constant axial force below 33N. The length and numbers of wires are chosen for practicality, as this will be the first actuator of its kind, and number of wires and length are readily scalable.

All units in SI units unless otherwise stated.

4 Energy Efficiency and Reliability

Approaching a relatively complex design, there has to be an engineer's selection of key aspects to take into account at first for various topologies.

4.1 Main Topics

4.1.1 Heat Loss

The specific heat capacity formula for liquids and solids without phase change provides a baseline figure for the energy consumption expected on actuation as well as how each particular element temperature delta may tax the system's energy efficiency. This implies treating them as isotropic homogeneous incompressible substances.

$$Q = m \cdot c \cdot \Delta T \tag{2}$$

where:

- m is body mass
- c is specific heat capacity
- ΔT is temperature variation

We can then particularize this equation for the kind of elements found in the actuator.

Tubing

$$Q = \rho \cdot \pi \cdot (\epsilon^2 + d_i \cdot \epsilon) \cdot L \cdot c \cdot \Delta T_h \tag{3}$$

where:

- ρ is density
- ϵ is wall thickness
- d_i is internal diameter
- L is longitudinal length

Rods or wires

$$Q = \rho \cdot \frac{\pi \cdot d^2}{4} \cdot L \cdot c \cdot \Delta T \tag{4}$$

Liquid Volume

$$Q = \rho \cdot V \cdot c \cdot \Delta T \tag{5}$$

With the SMA wire inside a liquid we need to establish how heat will propagate inside of it. The Biot number is a dimensionless quantity that may be used to asses if the temperature gradient between the inside of a body and its surface is relevant to lumped capacitance model of heat transfer calculations.

$$Bi = \frac{h \cdot L_C}{k} \tag{6}$$

where:

- h is film coefficient or convective heat transfer coefficient
- L_C is characteristic length
- k is thermal conductivity of the body

We find the characteristic length for an infinite cylinder to be defined in rough terms as $d/2$, as it is the distance of biggest temperature gradient inside this geometry, going from the central adiabat to the convection boundary, which is a fixed value on our design. Longitudinal length of the actuator will almost always comply with $L \geqslant 1000 \cdot d$. Natural convection of a liquid like water can be expected to be around $100\ \mathrm{W/m^2 \cdot K}$ giving:

$$Bi = \frac{100 \cdot 250 \cdot 10^{-6}}{18} = 1.38\hat{8} \cdot 10^{-3}$$

which falls well below the 0.1 reference figure at which you may expect lumped capacitance model calculation errors to be below 1%. The estimation for water's natural convection is not trivial and will be influenced by many factors during operation, but even for convection coefficients above 7000, which are figures typically associated with forced convection moderate flow of water in pipes, the SMA wire inner temperature gradient still can be disregarded.

To calculate theoretical efficiency limit for an SMA-based actuator around this wire we need to obtain input heat versus output work. Input heat comes from latent heat for phase transformation and temperature hysteresis width on SMA wires. For partial actuation knowledge about the amount of material experiencing the phase change would be needed, but for a full actuation we expect all the SMA to have gone into austenite phase. For a half cycle actuation energy per length is:

$$\frac{Q_{SMA}}{L} = \rho \cdot \frac{\pi \cdot d^2}{4} \cdot (\Delta H + c \cdot \Delta T) = 6500 \cdot \frac{\pi \cdot (500 \cdot 10^{-6})^2}{4} \cdot (24000 + 480 \cdot 40) = 55.13 \frac{\mathrm{J}}{\mathrm{m}} \tag{7}$$

This would be the theoretical minimum ammount of energy required for a single wire actuation, for a total of $110.3 \frac{\mathrm{J}}{\mathrm{m}}$ including a heating and a symmetric cooling process, and with no other material in the actuator experiencing the same temperature delta. Setting an actuation time target would set power requirements. For 1 second it would be 55.13 W/m for each process.

Work produced by a fixed wire being pulled by a constant external force would be given by the following equation:

$$W_a = e \cdot L \cdot F \tag{8}$$

where e corresponds to percentage of length actuated, which may be expressed per unit length:

$$\frac{W_a}{L} = e \cdot F = 0.04 \cdot 33 = 1.320 \frac{\mathrm{J}}{\mathrm{m}} \tag{9}$$

The external force would provide the other half of the actuation, as well as the previously provided heat being dissipated towards the surroundings. The energy efficiency intrinsic to an SMA actuator using this wire is:

$$\eta = \frac{W_a}{Q_a} = \frac{1.320}{55.13} \approx 2.3\% \tag{10}$$

Luckily, when an actuator is being used on an integrated exoskeleton, both power density and power-to-weight ratio come into consideration, as the exoskeleton has to be wearable and carried around, as well as reliable, easy to set up, having long life expectancies, where SMA-based actuators make a comeback.

For an actuator like the one mentioned before of 1 meter of length, which may be the required length for elbow actuation, supposing heating and cooling cycles are symmetric, ideal theoretical power density would be 6.7 MW/m^3 and specific power 1 kW/kg. For these figures to be directly comparable to other actuators, they would have to include Bowden tubing housing's, or other mechanical transmission supporting method's, weight, and acknowledge for the asymmetric heating and cooling processes, until now usually being Joule effect and air natural convection dissipation as previously mentioned, resulting in a quite fast contraction but not so fast relaxation .

Our goal will be to design a topology optimizing heating and cooling processes efficiency while reducing the number of elements/amount of material where ΔT_h is experienced. From a thermal mass point of view Volumetric Heat Capacity ($J/m^3 \cdot K$) points at what materials may be more taxing to our setup. Obtained from the following equation:

$$VHC = c \cdot \rho \tag{11}$$

We can compile a list VHC values of common engineering materials at a temperature around standard conditions:

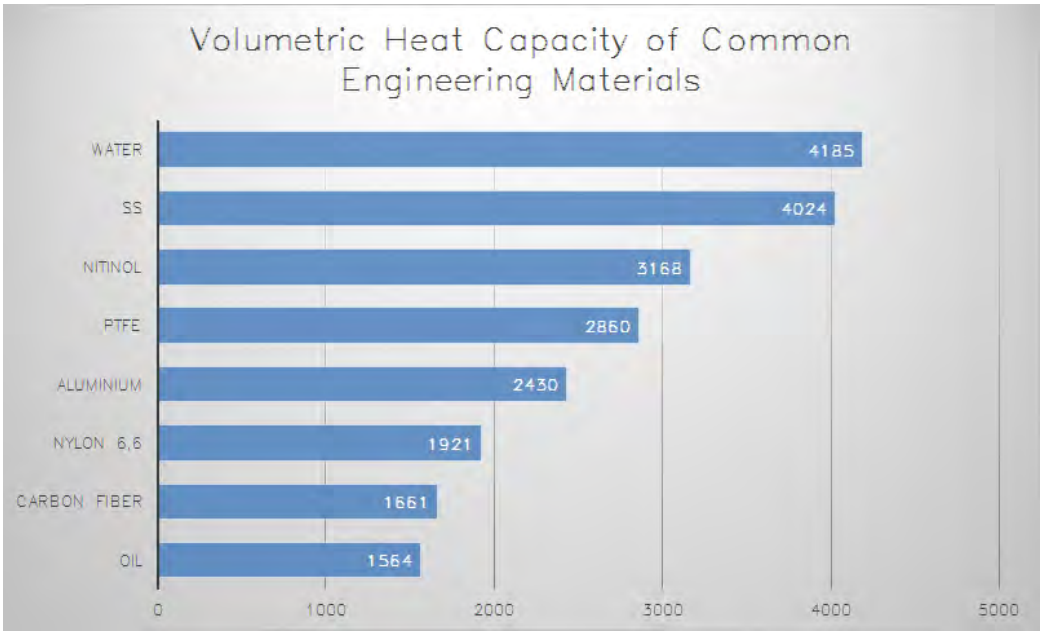

Figure 13: Volumetric Heat Capacity of Common Engineering Materials

4.1.2 Elastic Loss

Elastic energy will play a major role on the actuator's operation. Equations for area moments of inertia for the geometries found in the actuator are shown. All geometries are symmetrical, having the same area moments on x and y axis.

Tubing

$$I = \frac{\pi}{64} \cdot (d_o^4 - d_i^4) = \pi \cdot \left(\frac{1}{8} \cdot d_i^3 \cdot \epsilon + \frac{3}{8} \cdot d_i^2 \cdot \epsilon^2 + \frac{1}{2} \cdot d_i \cdot \epsilon^3 + \frac{1}{4} \epsilon^4 \right) \tag{12}$$

Rods and Wires

$$I = \frac{\pi}{64} \cdot d^4 \tag{13}$$

4.1.3 Locomotion

We will use three locomotion patterns to characterize the actuator's operation and the underlying energy efficiency:

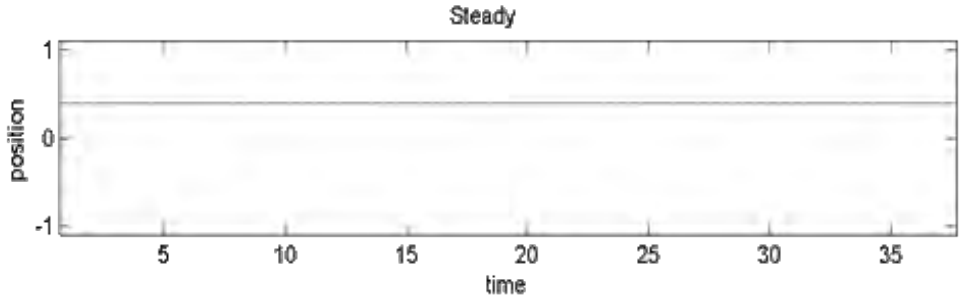

Figure 14: Steady Movement Position-Time Graph

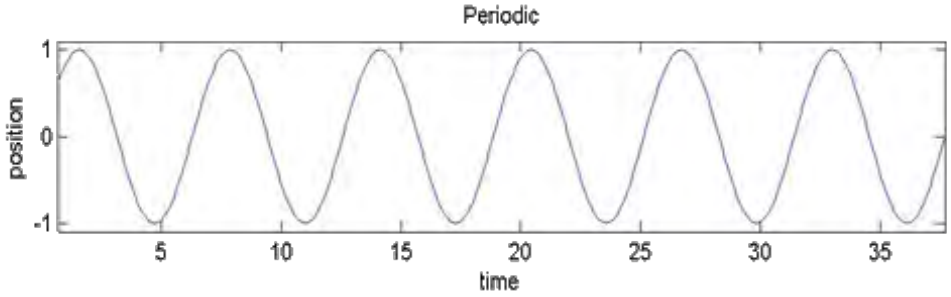

Figure 15: Periodic Movement Position-Time Graph

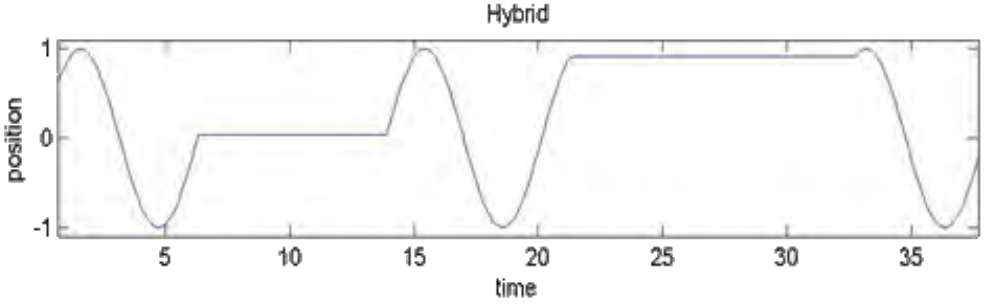

Figure 16: Hybrid Movement Position-Time Graph

A Fourier transform of a hybrid movement would just result in a fundamental frequency slower that the periodic segments present in it, implying slower periodic signals could convey the same information. For our actuator and its energy consumption this is not the case, having wildly different performance figures between holding position and any type of continuous locomotion.

4.1.4 Reliability

Finally, under the reliability tag, we will encompass relevant miscellaneous aspects of an actuator such as weight, assembly simplicity, MTBF figures, start-up time, etc.

4.2 Single Chamber Setups

This category presents a continuation on previous work, as the whole SMA wire is exposed to the same environment or surrounding fluid, specifically temperature-wise. Achieving both a continuous control of SMA wire's elongation while keeping energy efficiency and actuation time seems difficult given the governing thermodynamic equations.

4.2.1 Conservation of Energy

Conservation of energy transient equation for fluid on SMA chamber control volume as an open system with conservation of mass between input and output is:

$$\rho_f V_f c_f \frac{dT}{dt} = \dot{q} V_{SMA} - \dot{Q}_{CONV} + \dot{m}\big(c(T_i - T_o) + v(P_i - P_o)\big) \tag{14}$$

where:

- ρ_f average fluid density in temperature span
- V_f fluid available volume inside the chamber
- c_f average fluid heat capacity in temperature span
- $\dot{q}$ is internal heat generation from Joule effect
- $\dot{m}$ is mass flow rate
- v is specific volume
- T_x is absolute temperature at a given point
- P_x is absolute pressure at a given point

Temperature derivative over time assumes an average temperature for fluid inside the chamber. $\dot{Q}_{CONV}$ actually conveys both convection and radiation losses towards bowden tubing, which is a time dependent heat flow that can either be positive or negative, even if its surroundings are thermally

isolated, given bowden tubing's relatively high thermal mass. A preliminary time constant, $\tau = \frac{\rho V c}{h A_s}$, calculation below 1 second indicates that it will act as an electrical capacitor equivalent when actuation period is shorter or around that time, and the lumped capacitance model will hold true when actuation period is above 5τ . Later on this will be simulated through a numerically solved two dimensional equation, at this stage we will just acknowledge its occurrence as it is the same for all topologies.

Conservation of energy for actuator's closed system for a full heating cycle is:

$$\Delta E = Q_{SMA} - W_{SMA} + Q_{FLUID} + Q_{CONV} \tag{15}$$

where Q_{SMA} is SMA wire's actuation energy covered on Equation 7.

Conservation of energy for actuator's closed system for a full cooling cycle is:

$$\Delta E = -Q_{SMA} - W_{SMA} - Q_{FLUID} - Q_{CONV} \tag{16}$$

4.2.2 Variable Flow Speed

On this topology we are able to control flow speed using a external pump as shown on Figure 17. An external heat exchanger on the loop enables thermally isolating the SMA chamber, removing convection and radiation heat flow term.

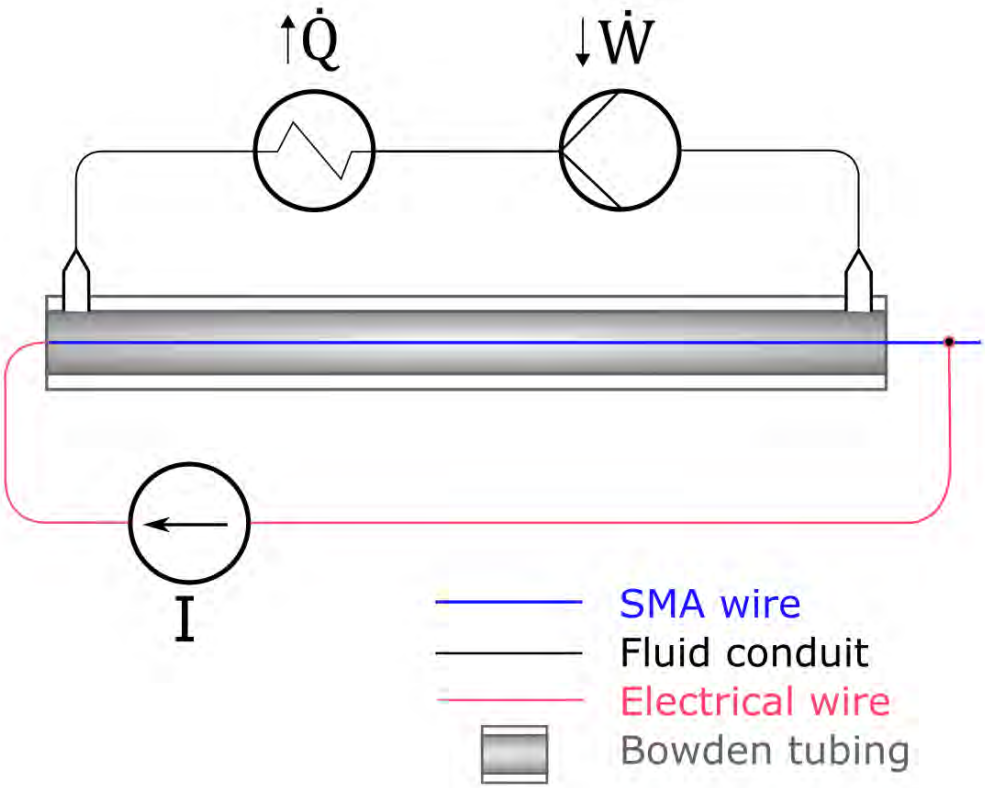

Figure 17: Variable Flow Speed Diagram

Equation for halted flow on heating cycle:

$$\rho_f V_f c_f \frac{dT}{dt} = \dot{q} V_{SMA} - \dot{Q}_{CONV} \tag{17}$$

Initially internal heat generation from an SMA wire would use part of this energy for its latent heat transformation. For rough estimations this can easily be disregarded when compared to the relatively large volume of the surrounding high volumetric heat capacity fluid.

Previous equation assumes that we are able to halt fluid flow on demand, but given the temperature gradient and associated relative pressure differences, that would allow for natural convection to happen, it may require additional check-valves at input and output of the bowden tubing.

Now for chamber's control volume cooling cycle:

$$\rho_f V_f c_f \frac{dT}{dt} = \dot{Q}_{SMA} - \dot{Q}_{CONV} + \dot{m}\big(c(T_i - T_o) + v(P_i - P_o)\big) \tag{18}$$

Energy stored, and corresponding heat flow, in SMA wire may be disregarded when compared to the relatively large volume of the surrounding high volumetric heat capacity fluid.

Right away you can see how such a topology would just increase system's thermal inertia, rendering it even less energy efficient. Depending on heat exchanger power dissipation this topology may or may not improve actuation time.

Conservation of energy for actuator's closed system for a full heating cycle is:

$$\Delta E = Q_{ACT} - W_{SMA} + Q_{FLUID} + Q_{CONV} \tag{19}$$

Conservation of energy for actuator's closed system for a full cooling cycle is:

$$\Delta E = -Q_{SMA} - W_{SMA} - Q_{FLUID} - Q_{CONV} + W_{PUMP} \tag{20}$$

This topology requires an external fluid conduit the same length as the actuator, as well as one pump per actuator and a radiator, reducing both power density and power-to-weight ratio. Controllability would be non trivial as repetitive starts and stops of the flow would generate a longitudinal temperature gradient on the actuator that would be slowly filled in by natural convection.

As an alternative a fluid demux may be used as seen of Figure 18, with heat being externally supplied to the wire. Even though this topology would just add complexity to the previous one with no real benefits, it served to put externally supplied heat into consideration.

Diving further into exotic topologies, it was considered a situation in which heat transfer fluid could be evacuated from the Bowden housing on demand. Although hard on both controllability and feasibility, it would remove added thermal inertia (Q_{FLUID}), obtaining current setup advantages with improved actuation time. Still into consideration for further research.

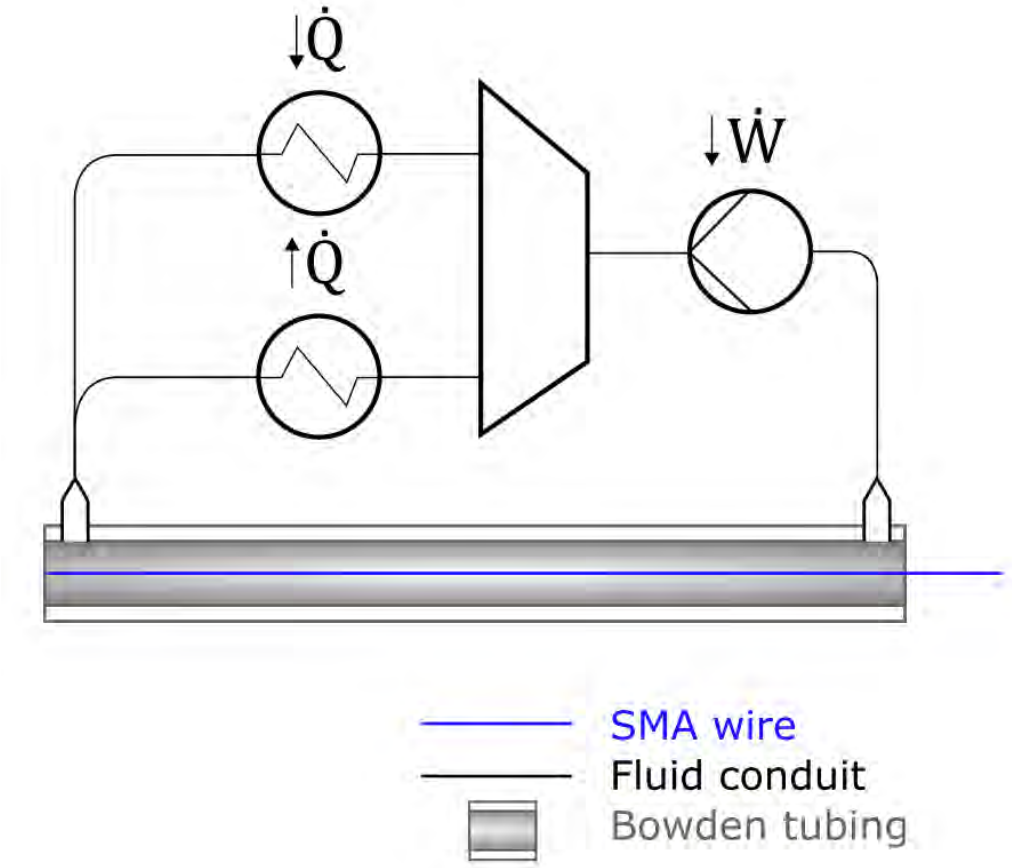

Figure 18: Dual Conduit Diagram

4.2.3 Bidirectional Flow

Using a fluid container a number of times bigger than the volume in the actuator as a buffer, and dual heat exchangers on the loop, this setup exploits the periodic quality of upper limb locomotion. Correctly sizing the container, chambering its insides exploiting natural convection to assure that hottest fluid would come out first when on heating cycle, and coldest would come out first on cooling cycle, using a electrically controlled heat extractor, like a Peltier module, would all be non trivial matters casting doubts on its feasibility.

Two pumps, a Peltier module with its heat sink and high volume container put this topology weight footprint at non-viable levels. Its precise controllability would also be quite the challenge.

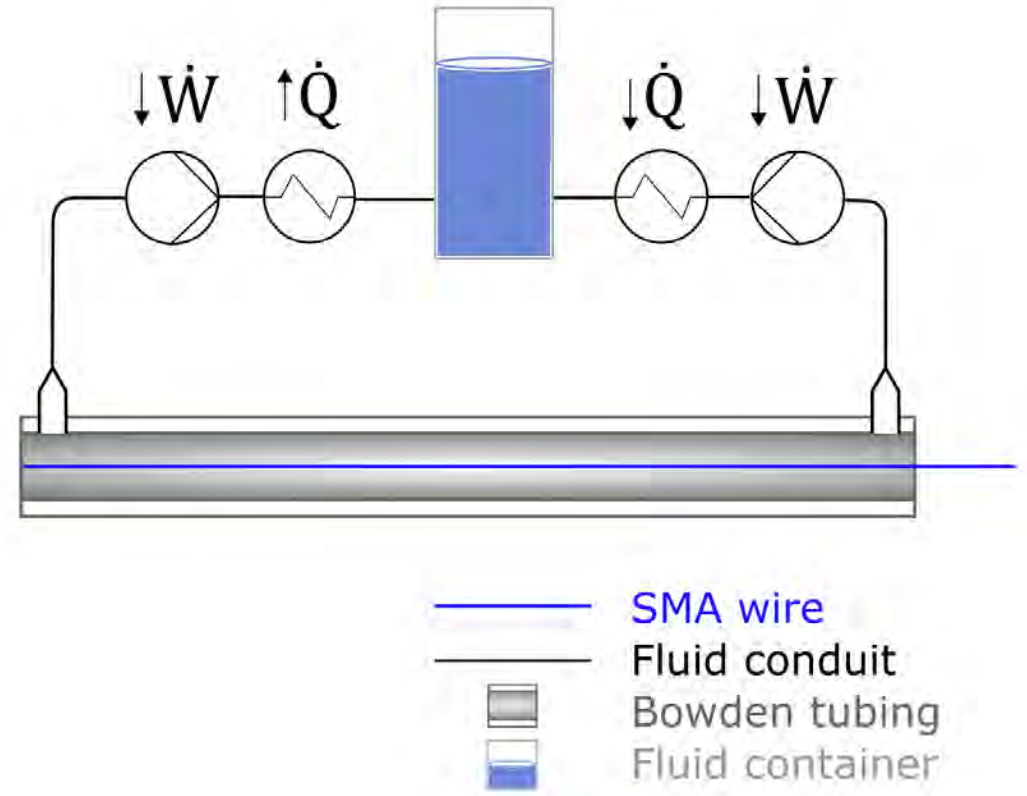

Figure 19: Bidirectional Flow Diagram

4.3 Split Chamber Setups

If we place an sliding watertight thermal isolator, or piston, inside a bowden-abled tubing, we are able to maintain a temperature delta comparable to that of the SMA hysteresis width. This allows for a section of the wire to be in austenite phase while the rest is in martensite phase.

This completely redefines the way elongation has been controlled up until now. Knowing the distance x of the thermal isolator from the higher temperature end, with a piston of length zero, percentage of austenite is expressed as:

$$A\% = \frac{x}{L} \cdot 100 \tag{21}$$

Not only may this simplify control architecture, it can also circumvent transformation temperature force dependence by just keeping high temperature side over A_f highest value, which would allow for seamless variable load control.

The piston will require for external actuation, the lower the energy footprint the better. This takes out of the equation high pressure setups like those seen on hydraulic linear actuators, instead an electrically actuated pulley seems like the best compromise. For capillary tubing there may be an option to use long bubbles, where buoyancy can be disregarded, but its position control won't be simple. [25]

Looking into the future of this actuator and converging with design needs, an antagonist actuator can be placed alongside. This has significant advantages:

- Fluid control volume remains constant, as when the thermal isolator moves, fluid will just flow in or out the same cross section of tubing.
- From a mechanical perspective, moment of inertia doesn't change, as opposed to when filling or emptying a container on an end of the actuator
- Bowden force transmission is split between both tubes
- Moving closer to a final product

4.3.1 Conservation of Energy

Conservation of energy transient equation for high temperature (HT) chamber fluid's control volume is:

$$\rho_f V_f c_f \frac{dT}{dt} = \dot{q} V_w - \dot{Q}_{SMA} - \dot{Q}_{ISO} - \dot{Q}_{CONV} \tag{22}$$

$\dot{Q}_{CONV}$ has been covered at section 4.2.1. $\dot{Q}_{ISO}$ is heat loss through the sliding thermal isolator, either through longitudinal conduction or from lossy watertightness. Internal generation comes from a heating element submersed in fluid.

Opportunely this equation would only happen during start-up of an actuator, when heat transfer fluid is at ambient temperature, resorting to $\dot{q} V = \dot{Q}_{SMA} + \dot{Q}_{ISO} + \dot{Q}_{CONV}$ on steady state .

Conservation of energy transient equation for low temperature (LT) chamber control volume as an open system is:

$$\rho_f V_f c_f \frac{dT}{dt} = \dot{Q}_{SMA} - \dot{Q}_{CONV} + \dot{m}\big(c(T_i - T_o) + v(P_i - P_o)\big) \tag{23}$$

LT benefits from having the smallest thermal resistance to ambient temperature.

Conservation of energy for HT chamber's closed system for a heating cycle is:

$$\Delta E = Q_{SMA} - Q_{CONV} \tag{24}$$

Conservation of energy for LT chamber's closed system for a cooling cycle is:

$$\Delta E = -Q_{SMA} - Q_{CONV} \tag{25}$$

4.3.2 Longitudinal Conductivity

This setup tries to exploit the highly convective characteristics of heat propagation on a small volume of liquid to supplement low thermal conductivity on heat-transfer liquids.

Natural convection can be studied by obtaining the dimensionless Rayleigh number, which is defined as a product between Grashof and Prandtl number, or ratio of buoyancy and viscous forces multiplied by ratio of momentum and thermal diffusivities.

$$\mathrm{Ra} = \mathrm{Gr} \cdot \mathrm{Pr} = \frac{g \beta D^3}{\alpha v} \tag{26}$$

where :

- g is local gravitational acceleration
- β is volumetric thermal expansion
- D is characteristic length of a pipe, or loop size
- α is thermal diffusivity
- v is kinematic viscosity

Values α, β, v obtained at the film layer.

To validate Rayleigh value we would need the respective Nusselt value, the ratio of convection to pure conduction.

$$\mathrm{Nu} = \frac{hL}{k} \tag{27}$$

Calculating representative Ra and Nu numbers is non-trivial, and there are great drawbacks to this type of heat transfer right from the start. First, as seen from Ra equation, it depends on an external acceleration, usually g. For an actuator that may be in any given orientation, and even moving with comparable acceleration due to body locomotion, buoyancy dependence seems troublesome. Secondly, long linear displacement will disassemble convection loops, that added to the longitudinal length will result in a delay of heat transfer to an from the SMA wire.

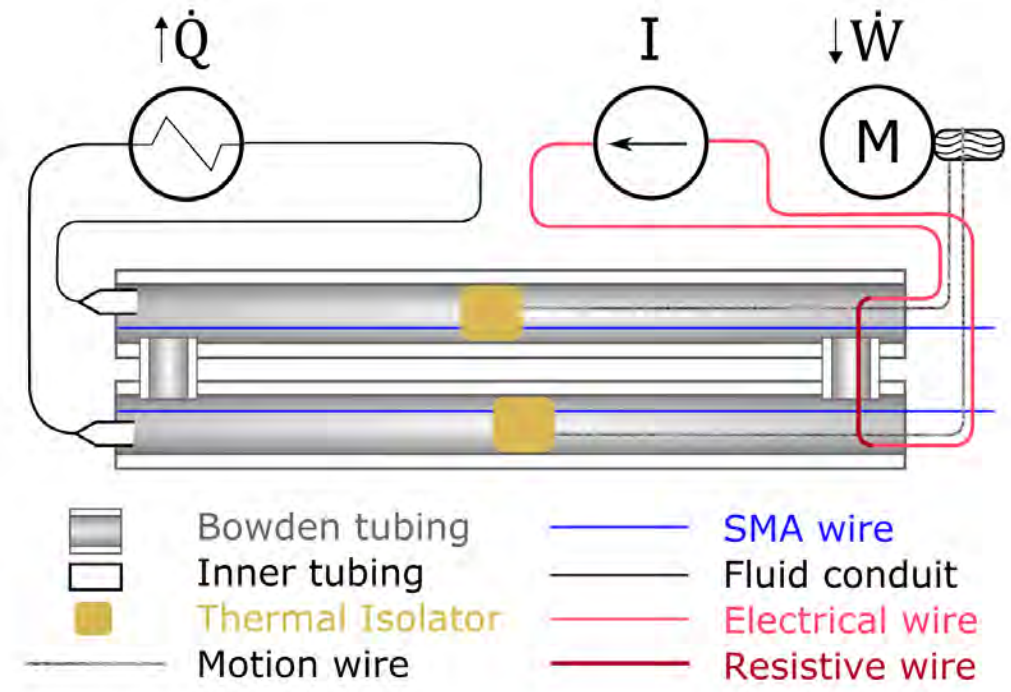

Figure 20: Longitudinal Conductivity Diagram

A well researched method for passive heat transfer are **heat pipes**. Although extremely efficient and reliable, it would prove a challenge to integrate a sliding thermal isolator, attributable to their high design complexity, and weight and manufacturing cost end up tipping the scale away from this approach.

4.3.3 Uniform Cross Section

On this topology we shift a thermal problem to a fluid mechanics one. A pulley system is arranged inside the bowden tubing to both actuate the piston, and have a relatively uniform thermomechanical cross section that avoids longitudinal heat transfer disadvantages.

Two elements enable this behaviour, a flexible resistive wire, for HT side, and a flexible inner tubing with holes at its ends, for LT side. On HT side, the mean distance to a heat source will be smaller or equal to $\frac{d}{2}$, added to previously explained natural convection, for high enough heating power, heat transfer delay can be disregarded. On LT side, a controllable speed fluid flow enters one actuator's bowden tubing, goes over this actuator's SMA wire, jumps into the inner tubing, exits next to the other actuator's piston, goes over the SMA wire and exits the bowden tubing towards pump and heat exchanger

Apart from the watertight pistons, we also need to restrict fluid flow around the inner tubing at LT chambers' junction. Watertightness comes at the expense of friction losses, that will be present also for piston actuation. Lossy watertightness on piston would result in advection losses, on inner tubing restriction would just increase transient towards LT chamber steady state when the piston is moved, diregarded for energy efficiency calculations.

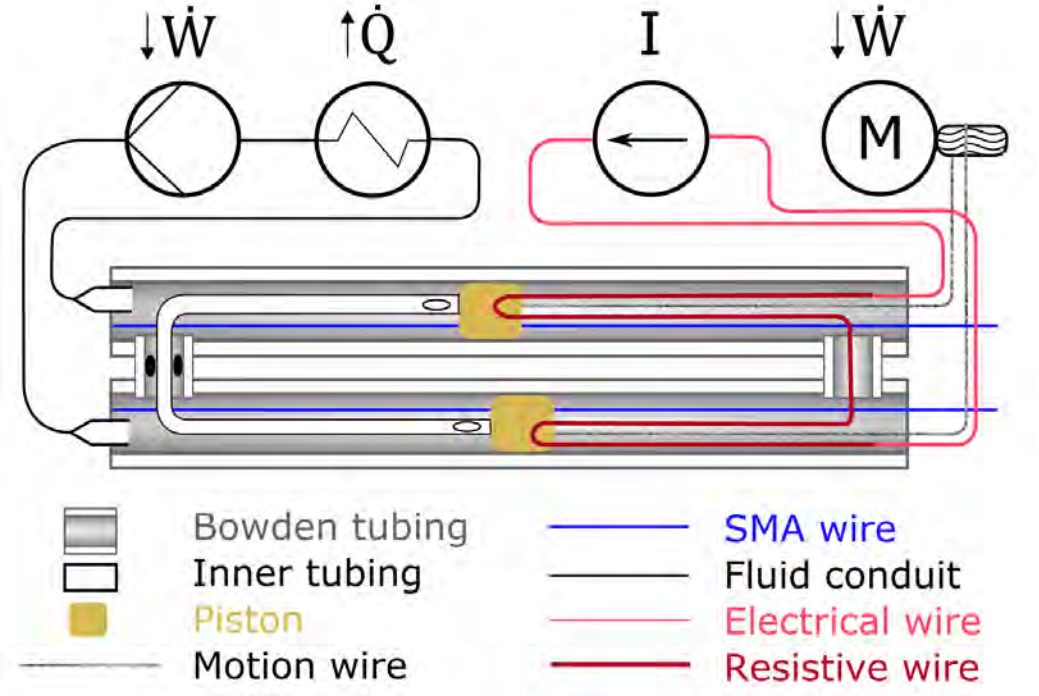

Figure 21: Uniform Cross Section Diagram

This topology uses one pump, with the associated low MTBF, and an external heat exchanger, both shareable between a number of actuators, a motor and a pulley, that may be miniaturized, but definitely targeting its power density and power-to-weight ratio.

Actuation time now depends on piston's speed inside the tubing, and controllability on piston's position which by default has great resolution as its movements across the wire are attenuated on the output about 25 times by SMA elongation percentage.

Conservation of energy transient equation for HT chamber control volume is:

$$\rho_f V_f c_f \frac{dT}{dt} = \dot{q} V - \dot{Q}_{SMA} - \dot{Q}_{ISO} - \dot{Q}_{CONV} \tag{28}$$

Conservation of energy transient equation for LT chamber control volume as an open system is:

$$\rho_f V_f c_f \frac{dT}{dt} = \dot{Q}_{SMA} - \dot{Q}_{CONV} + \dot{m}\big(c(T_i - T_o) + v(P_i - P_o)\big) \tag{29}$$

Conservation of energy for the complete agonist-antagonist actuator as a closed system during a heating cycle is:

$$\Delta E = (Q_{SMA} + Q_{BOWDEN}) - (Q_{SMA} + Q_{BOWDEN}) - 2 \cdot W_{SMA} - Q_{CONV} + W_{PUMP} + W_{PULLEY} \tag{30}$$

where W_{PULLEY} is piston actuation, comprised by work performed, friction losses, elastic losses, motor efficiency, etc.

From here we can compile this topology's energy efficiency equation

$$\eta = \frac{2 \cdot W_{SMA}}{Q_{ACT} + W_{PUMP} + W_{PULLEY}} \tag{31}$$

Denominator terms are to be minimized through mechanical design and control strategies.

Q_{ACT} covers:

- SMA actuation energy, Q_{SMA}, fixed by manufacturer.
- Dissipation losses towards the surroundings, which can be inhibited by a Dewar vessel inspired solution.

- Bowden tubing wall heating, Q_{BOWDEN}, which can be restrained if a compound structure is devised, having a low thermal constant thin-walled container supported by a high compressive strength array.

W_{PUMP} depends on:

- Pump's energy efficiency, designed by manufacturer.
- Primary and minor losses, that rely on tubing geometry and fluid selection.
- Control Strategy, disabling the pump when heat exchanging is not needed.

W_{PULLEY} is the most mechanically design dependent term, encompassing:

- Piston actuation, which is a summation of friction from both watertight pistons, inner tubing fluid restriction and interfaces for SMA wires and motion wire; elastic energy of inner tubing, heating element and motion wire; parasitic losses like fluid viscous movement.
- Electric motor's energy efficiency and pulley slip over motion wire
- Control strategy, given highly non linear piston actuation force equation.

5 Mechanical Design

After prior analysis, uniform cross section topology is deemed as the superior candidate for empirical implementation.

Each element of the system has been specifically chosen for the application at hand, trying to prototype the best working solution while minimizing price, meaning using custom parts only when necessary, trying to fit already available industry solutions.

Although sections are arranged in a certain fashion to improve readability, design process required all parts to be developed at the same time, being heavily dependent on one another, to avoid getting constrained further down the line.

5.1 Heat-transfer Fluid

Fluid selection is derived mainly from pressure drop on the piping of LT chamber. For major losses dependent pressure drop we need to establish the type of flow inside the tubing. The dimensionless Reynolds number gives a ratio between inertial and viscous forces.

$$\mathrm{Re} = \frac{u_m d_h}{\nu} \tag{32}$$

- u_m is mean velocity
- d_h is hydraulic diameter
- ν is kinematic viscosity

Reynolds number critical values are empirically established at 2300 and 4000. Below 2300 laminar flow prevails, above 4000 turbulent flow dominates, between those values there is a transition between laminar and turbulent flow.

There are two cross sections for fluid flow, hydraulic diameter and velocity will differ between both, the first defined as $d_h = \frac{4A}{P}$, the second obtained from $u_m = \frac{Q}{A}$ volumetric flow rate over area.

Stating hydraulic diameter equation for our geometries, a mostly circular one inside inner tubing, where $d_h = d_i$, and an annular one around inner tubing, where $d_h = D_i - d_o$.

From conservation of linear momentum in a control volume:

$$\frac{d}{dt}\left[\int_{V_C}\rho\,\bar{v}\,dV\right]+\int_{\Sigma_C}\rho\,\bar{v}(\bar{v}-\bar{v}_c)\bar{n}\,d\sigma=-\int_{\Sigma_C}p\,\bar{n}\,d\sigma+\int_{\Sigma_C}\bar{\tau}'\bar{n}\,d\sigma+\int_{V_C}\rho\,\bar{f}_m\,dV \tag{33}$$

When steady state is reached and there is a fully developed fluid flow, left side terms are zero. Further solving with a longitudinal differential term, pressure drop can be stated as:

$$\Delta P=\frac{1}{2}\rho\,u_m^2\frac{\lambda L}{d_h} \tag{34}$$

where λ is coefficient of friction, that for a turbulent flow may be estimated from Moody's Diagram. When flow is laminar, there exists a direct relationship between λ and Re:

$$\lambda=\frac{64}{\mathrm{Re}} \tag{35}$$

reducing pressure drop equation to:

$$\Delta P=32\mu\,u_m\frac{L}{d_h^2} \tag{36}$$

where μ is dynamic viscosity, $\mu=\nu\cdot\rho$, SI units Pa·s, but usually given in centipoise, or cP, 1000cP $=1\mathrm{Pa}\cdot\mathrm{s}$. Dynamic viscosity varies greatly with temperature for almost any fluid as seen on Figures 22 and 23.

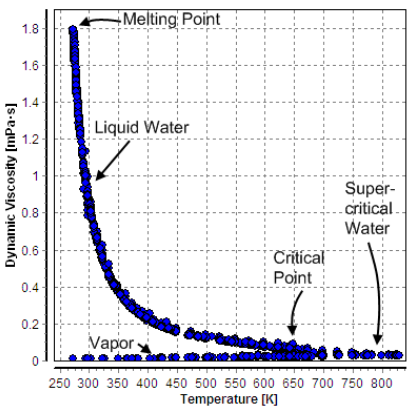

Figure 22: Dynamic Viscosity of Water [22]

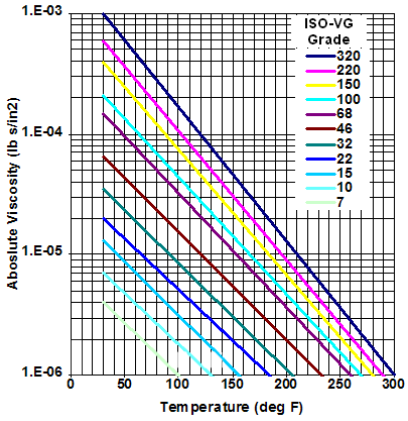

Figure 23: Dynamic Viscosity of ISO-VG Grade Oils [23]

Even though geometrical inconsistencies and fluid flow compression, expansion and turning will affect flow development, values obtained from these

equations will provide a good enough approximation, that later on will be tested.

Preliminary calculations of Re using water as heat-transfer fluid indicate that annular section tubing will almost always be inside laminar flow region, set values upper bounded at 1280. Inner tube section Re number depends much more on geometry, placing itself either on transition region or on turbulent region depending on flow rate. We are interested in worst case scenarios, so we will take $\lambda = 0.05$ for our smooth pipe.

Associated pressure loss for L = 0.5 m on annular section will be upper bounded at 1 kPa; on the contrary, inner tubing section presents concerns, as pressure drop can go above 30 kPa as diameter is reduced, due to its quadratic relation with fluid velocity. Although cavitation due to reaching saturation should not be a concern on a closed cycle like ours, electric pump has an inverse relationship between flow and pressure drop, meaning a higher pressure drop would restrict flow, reducing fluid flow heat transfer capabilities.

At the same time minor losses also depend on mean velocity different between sections. Equation for fluid flow contraction is:

$$\Delta P_{mc} = \frac{1}{2}\rho[u_i t^2(1-K_c)+u_{an}^2] \tag{37}$$

where:

- K_c is contraction loss coefficient, value bounded to $[0, 0.5]$.
- u_{it} is velocity inside inner tubing section.
- u_{an} is velocity inside annular section.

And for fluid flow expansion is:

$$\Delta P_{me} = \frac{1}{2}\rho[u_i t^2(K_e+1)-u_{an}^2] \tag{38}$$

where K_b is contraction loss coefficient, value bounded loosely bounded around $[0.1, 1.1]$.

Having both in series, supposing no interaction between them results in:

$$\Delta P_m = \frac{1}{2}\rho\, u_{it}^2(K_e+K_c) \tag{39}$$

Characterization of contraction and expansion coefficients having three dimensional interactions is non-trivial. At this point we will just establish that ΔP_m can be up to 5 kPa for a fluid like water.

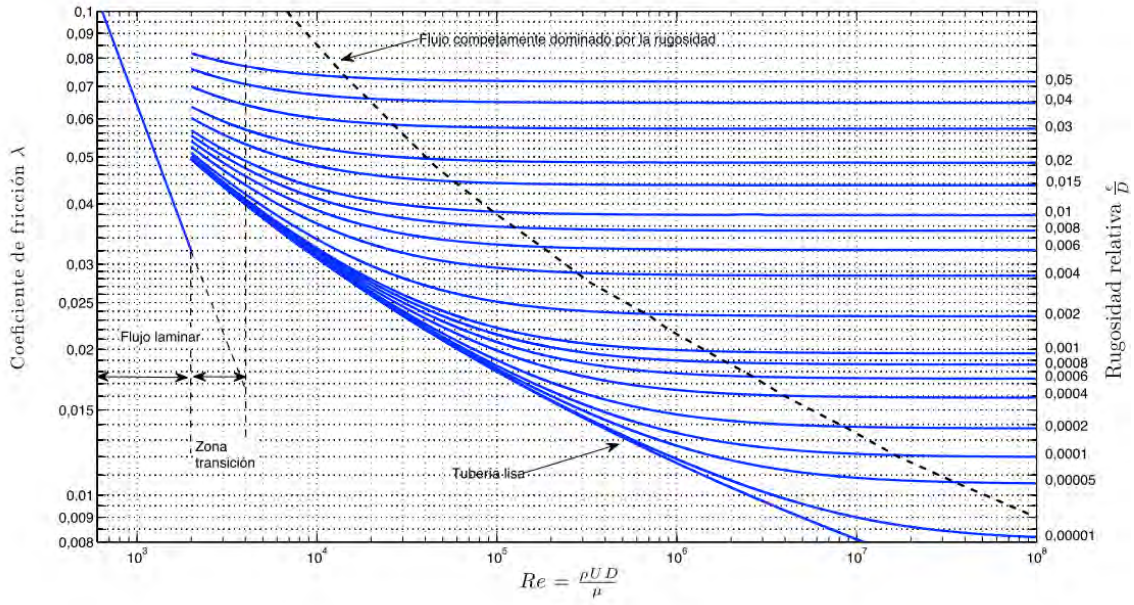

Figure 24: Moody Diagram [24]

Interest on diameter reduction is explained on Inner Tubing chapter.

Exploiting non linear behaviour around this Re values , slightly increasing fluid's absolute viscosity may found a minimum on pressure drop, maximizing flow rate, by pushing it into laminar flow. At the same time, increased absolute viscosity makes things easier on liquid-liquid and liquid-air watertight interface.

Looking now at HT chamber, fluid also needs to provide thermal transfer axially, which won't be a problem thanks to the uniform cross section, as explained on chapter 4.3.2. Additionally fluid's electrical conductivity is to be minimized, as it could present a parallel path to resistive wire.

Dynamic viscosity temperature dependence shown on Figures 22 and 23 results in having quite differently performing fluids on each side of the piston. This could be compensated by using different fluids, like various VG Grade oils, having its own practical implications.

Other parasitic effects are high heat capacity fluid like water can slightly improve actuation time by releasing its own heat when required, instead of

depending on heat flow from resistive wire. At the same time, advection losses due lossy watertightness, for the same volume will have a higher cost for high heat capacity fluids, from Equation 5.

At this stage of development, for implemented geometries, distilled water fulfilled the requirements and was chosen for its obvious practicality.

5.2 Liquid-Liquid Interface

This elements sets most of the geometrical constraints for the rest of the setup due to its multiple function integration.

Thermal isolator limiting heat flow between chambers.

Watertight division impeding heat-transfer fluid advection across chambers while allowing SMA wires to traverse it.

Heating Element Support needed on uniform cross section topology

Belt Link enabling its actuation

And it has to perform this functions, specially watertightness with the least amount of friction possible.

An industry standard for this kind of application are o-rings, toroidal gaskets, usually made out of an elastomer, that are compressed between solid materials resulting in compartmentalization from one side to the other.

The dimensionless parameter governing its performance is compression set or squeeze [26]:

$$\text{Squeeze} = 1 - \frac{gl}{CS} = 1 - \frac{D_i - GD}{2 \cdot CS} \tag{40}$$

where:

- CS is torus cross section diameter.
- gl is gland depth.
- D_i is water container inner diameter.
- GD is piston groove diameter.

GD usually matches ID, torus inner diameter, slightly overshooting it to pre-strech the oring [26], but this is one parameter we will have to fiddle with to tune frictional forces. Other oring parameters are material, each with its own set of chemical compatibility and temperature range, and hardness, specified by a two-digit Shore A durometer number.

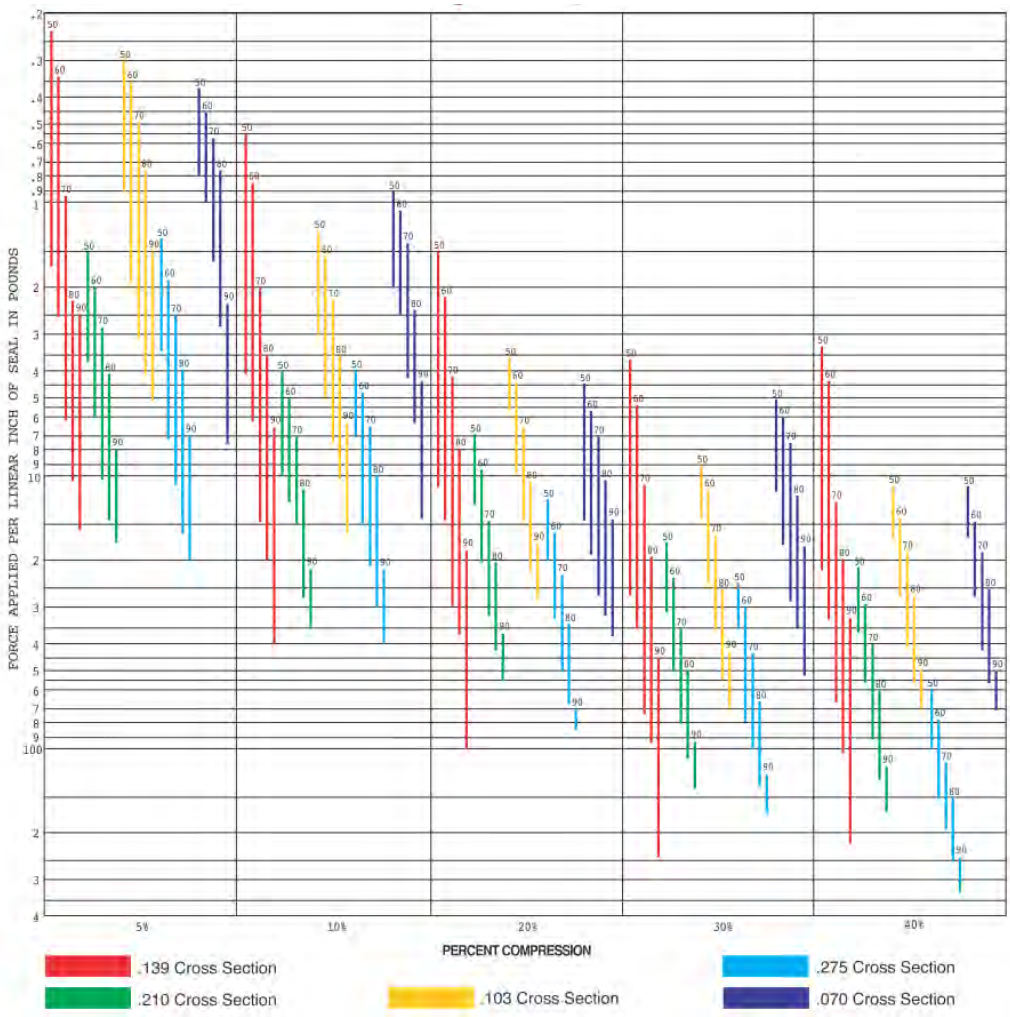

Figure 25: Seal Compression Design sorted by CS and Hardness[26]

From Figure 25 and o-ring availability we could choose a percent compression, and apply Coulomb friction model, $F_r = \mu_r F$ to obtain a reference value of expected friction, which served as a starting point, but the limitations to this approach are many.

For a start, there is a notable difference between an industrial application and ours, which is that the container, also bowden tubing, is a rather easily de-

formable solid. Then there are tolerances, on bowden tubing inner diameter and ovality, on oring cross section, on our piston groove, etc. that affect oring's compression set. For our small geometries, extruded pneumatic PTFE tubing manufacturing tolerance is on the verge of unsuitability, and offered inner diameters stepping from 2mm to 4mm to 6mm heavily restricted employable oring sizes fitting target compression set. And finally, being a dynamic seal targeting a small compression set where hydrodynamics play a role, it falls in a gray area.

Together with Technical Office we decided an iteration approach would yield best results, empirically testing different piston grooves depths and diameters for fixed o-ring and Bowden tubing.

The objective for piston skeleton design is to maximize available inner area for SMA wires to go through as seen on Figure 26. This area will be constrained by maximum piston diameter and minimum groove depth, dot line on Figure.

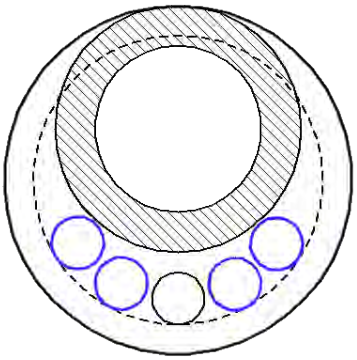

Figure 26: Piston Multiwire Profile

Piston skeleton should not scrape against walls, being strictly smaller than D_i minus tolerance over ovality factor, setting the maximum piston diameter. Ovality factor was unavailable, relying on empirical testing it was established at 1.031 for our tubing. Piston diameter was fixed at 5.65mm.

Piston's diameter is associated to its length when considering a certain minimum Bowden tubing bending radius.

$$l_{max} = \sin\left(\arccos\left(\frac{w - D_i + e}{R} + 1\right)\right) \cdot 2R - 2e \tag{41}$$

where:

- w is piston diameter
- D_i is Bowden tubing diameter
- e is minimum clearance, that has to take into account D_i tolerance, ovality, and a security margin.
- R is minimum Bowden tubing radius

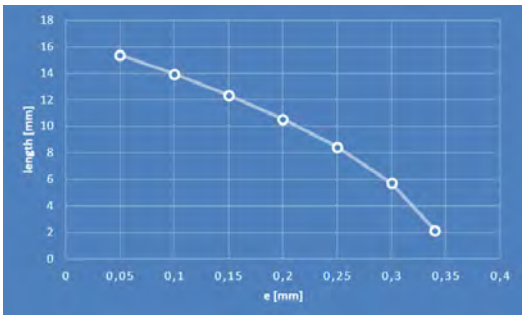

Figure 27: Piston Length vs Minimum Clearance Graph

All parameters on l_{max} equation are fixed except for minimum clearance. A plot of its non linear evolution can be seen on Figure 27. It was decided 0.2 mm of margin, to cover for ±0.15 Bowden diameter tolerance.

Ratio of groove depth, that contains the oring, and gland depth, distance from bottom of groove to wall, should be kept above 75% at all times [26], setting minimum groove depth. If this condition is not met the oring may be able to exit the groove ruining its functionality. Counterintuitively, the bigger the groove diameter, which increases compression set, the smaller the ratio becomes. We managed to operate around 70% with careful assembly of the actuator.

Bringing all this together, we purchased high quality HNBR orings, size ID 4.7 / CS 0.7 / OD 6.1, trying to maximize available inner area as explained, and targeting a compression set below 10%. Test pieces with varying grooved depths shown in Table 4 were manufactured on PVC and results are shown in the analysis chapter.

Table 4: Compression Set Minimum, Nominal and Maximum

GD[mm]	MIN	NOM	MAX
4.80	-5	14	29
4.75	-9	11	26
4.70	-13	7	23
4.65	-17	4	20
4.60	-21	0	17
4.55	-25	-4	13
4.50	-29	-7	10

To complete an SMA wire watertight interface we used stainless steel hypodermic needles. 21 gauge needle inner diameter corresponds to 0.514 ± 0.019, outer diameter being 0.8192 ± 0.0064 [27]. Friction coefficient between metals is quite low, resulting in a friction force below 0.5N. Watertightness was tested with 90°C water with small pressure differentials with good results in

static and slow movement speeds, high speed displacement would require additional testing to quantify tolerance dependence.

Due to machinability, temperature working range and thermal conduction requirements the skeleton shown in Figure 26 was made out of PTFE. Other available plastics like PVC would work around their glass transition temperature, possibly losing some of their mechanical properties, as transition starts below T_g listed temperature.

Thermal isolation is approximated from one dimensional heat conduction equation as a thermal resistance.

$$R = \frac{L}{kA} \tag{42}$$

where:

- L is mean longitudinal path
- k is thermal conductivity
- A is wet area

There are multiple thermal resistances in parallel, piston skeleton, oring, needle. Both skeleton and oring are made out of a low thermal conductivity plastic, around 0.24 $\frac{\mathrm{W}}{\mathrm{mK}}$, while needle has 20 $\frac{\mathrm{W}}{\mathrm{mK}}$ from stainless steel.

From rough mean longitudinal path calculations a value around 150 K/W is obtained, which would allow a heat flow of 270 mW if temperature delta was SMA hysteresis width. This aspect definitely allows for further improvement and in-depth analysis, but mechanical aspects presented a much bigger concern at this point, not being worth spending time further analysing thermal aspects when geometries are prone to change.

Heating element support is covered in its own chapter.

Belt link features mechanical connections given the difficulties to stick anything to PTFE, using a pass through hole where a knot can hold motion wire from LT chamber, and a knob where inner tubing can fit and be secured with a small transversal metallic retainer. Linear actuation force of belt setup is expected to be kept below 20 N.

Finally we arrive at a piston sketch fulfilling all the previously mentioned conditions.

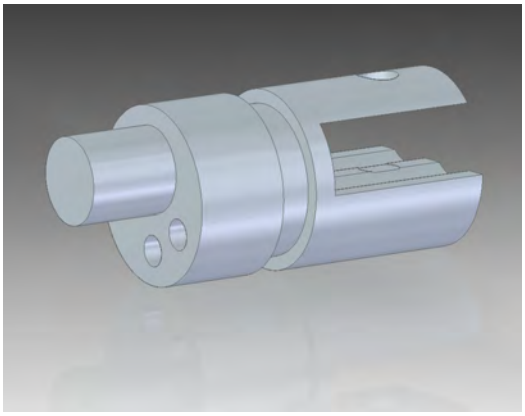

Figure 28: PTFE Piston Skeleton

And a fully assembled one:

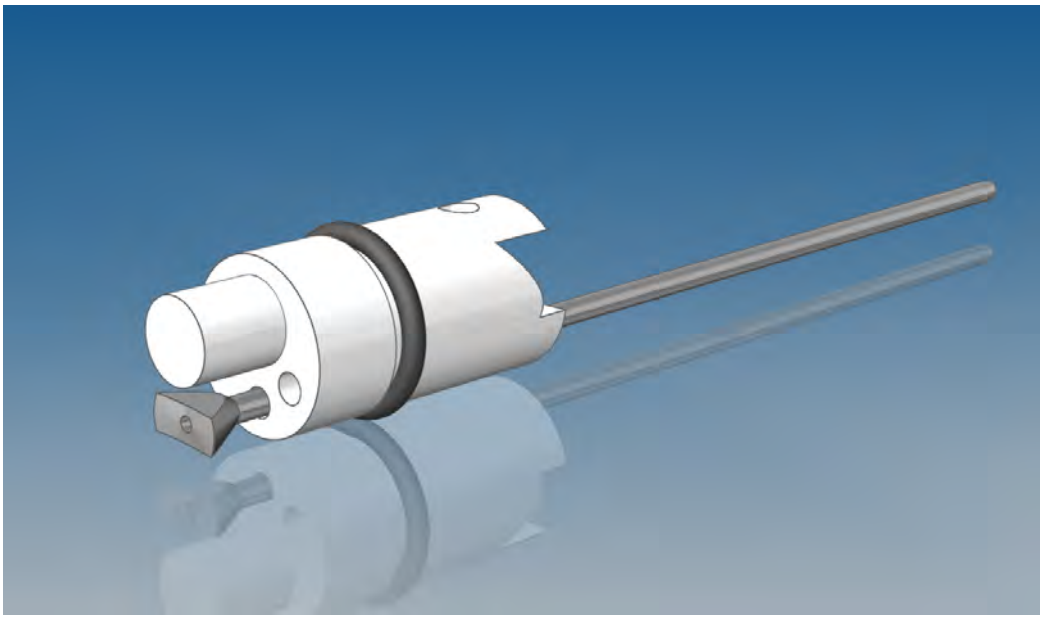

Figure 29: Assembled Piston with O-ring and Needle

5.2.1 Lubrication

An interesting component to reduce friction while not affecting watertightness is lubricating or greasing inner walls, o-rings and inner tubing. This provides an elastohydrodynamic film for components to slide onto.

We searched for a grease with wide temperature range and great resistance to water wash-out. This is tested through DIN 51807, where our grease obtains complete water resistance.

Relying on lubrication for staying in operating range may affect actuator's MTBF figure, as continuous operation may end up pushing most of it to the ends of the Bowden tubing, with film's linear profile following an inverted Gaussian curve.

5.3 Air-Liquid Interface

Present at the end of both chambers, they allow for an SMA wire to move through while maintaining watertightness.

Needles were already covered on the previous section. As the main driving force for water egress is a pressure differential, with both sides at roughly the same atmospheric pressure during operation, and SMA wire limited displacement, it is unlikely that fluid is lost here. For motion wire on HT side, as said for higher speed displacement, it needs further testing.

Being exposed to the same conditions than the piston we resort to PTFE for their skeleton. On HT chamber they allow for heating element electrical wire access, on LT chamber it is also inner tubing path to and from pump and radiator.

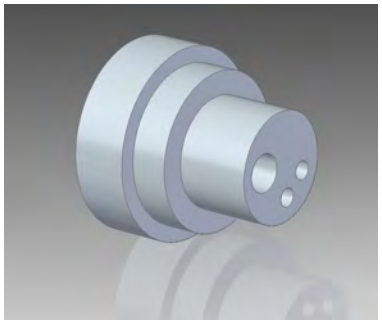

Figure 30: PTFE HT End Skeleton

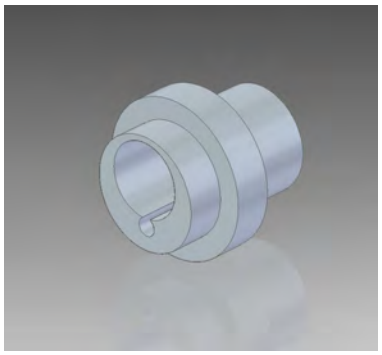

Figure 31: PTFE LT End Skeleton

Fully assembled they look like this:

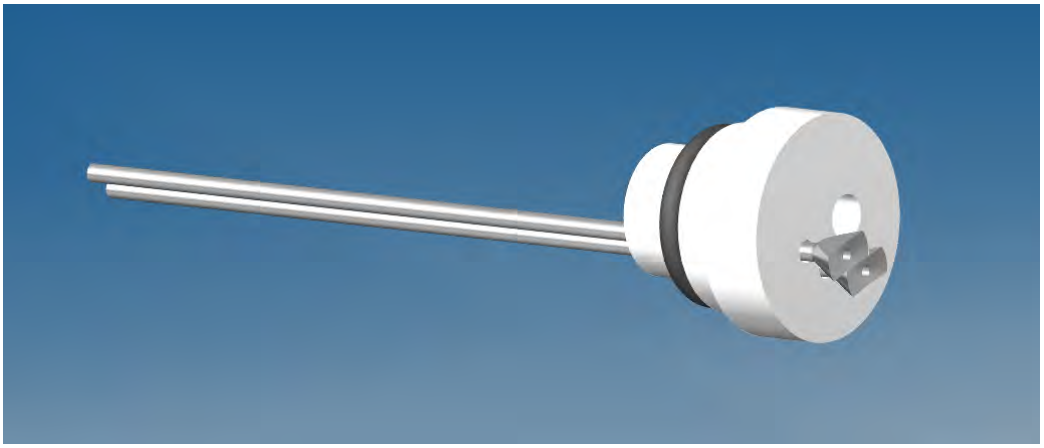

Figure 32: Assembled HT End with O-ring and Needles

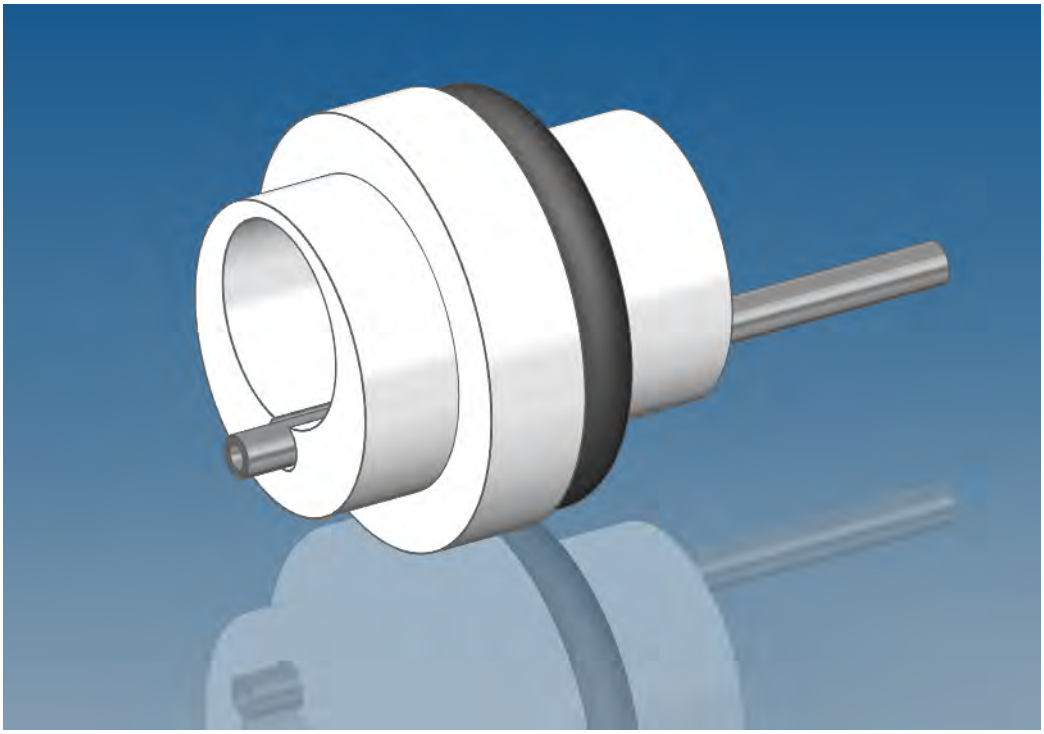

Figure 33: Assembled LT End with O-ring and Shortened Needle

5.4 Bowden Tubing

Bowden cable is a mechanical force transmission method where a cable is constrained inside a hollow longitudinally incompressible tubing, usually steel helical windings, that are conformable. On one end cable is fixed to the hollow tubing, using a barrel adjuster, the other end pulling on a load. Cable slides with low friction inside the tubing allowing for great efficiency.

Any SMA-based actuator long enough will have to make use of bowden tubing for mechanical tranmission to keep some of its flexibility. As shown on Figure 11, the automotive industry standard for bowden tubing, stainless steel, has great volumetric heat capacity and density, so this is an area where application specific improvements can be achieved.

The solution proposed is to have an element share the funcionality of fluid container and bowden tubing, at first using an homogeneous one like, already available industrywide, PTFE pneumatic tubing. Moving to a plastic Bowden tubing means having to look at its compressive strength and at its heat deflection point, that may result in output work loss, due to lower compression modulus, and cast problems on its structural integrity.

Even worse could be the buckling modes present on such slender tubing. From Euler's critical load equation:

$$F = \frac{\pi^2 \cdot E \cdot I}{(K \cdot L)^2} = \frac{\pi^2 \cdot 0,4 \cdot 10^6 \cdot 1,37 \cdot 10^{-10}}{(1 \cdot 0,5)^2} = 2,2\text{N} \tag{43}$$

But as this works as a bowden tubing, the inner tensioned SMA wires restricts these failure modes, as was empirically tested, having to deal only with its compression modulus and its heat deflection point.

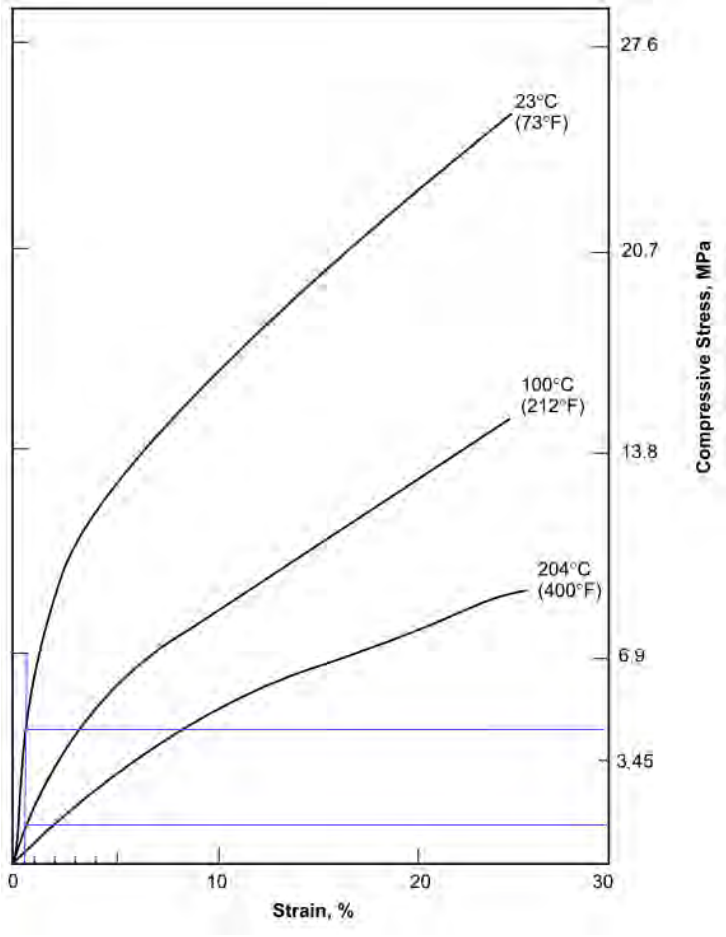

Figure 34: Compressive Stress-Strain for PTFE [38]

For this prototype 6 ID / 8 OD tubing seems like the best compromise between weight and feasibility, covered on Liquid-Liquid Interface section. On Figure 13 we can see a reference table of compressive stress vs strain at different temperatures. Blue lines represent 0.5% strain at 23 °C and 100 °C, with our setup high temperature side hovering around 75 °C. On an antagonist setup, total load is distributed between both tubes axially, pressure would then be:

$$P = \frac{F}{A} = \frac{33}{2 \cdot 2,2 \cdot 10^{-5}} = 0,3\text{MPa} \tag{44}$$

For this setup we are inside the operating region with a notable factor of safety, needed for extruded PTFE, as was also tested with maximum load. But looking towards increasing loads supported by this tubing, trying to contain the elastic strain limits below 0.5% for the temperatures mentioned, compressive stress falls under 2 MPa, with a maximum force of:

$$F = P \cdot A = 1,8 \cdot 10^6 \cdot 2,2 \cdot 10^{-5} = 79,2\text{N} \tag{45}$$

This would be a major limitation for a multiwire actuator, as adding diameter and/or thickness to supplement for this would bring down power density and power-to-weight ratio. There are also concerns of structural integrity when one tube is under full actuation at high temperature, being slightly shortened, and the other tube is expected to support part of the load, with no tension through its wires that may allow in the long run for buckling to take place, further reducing the load limit.

This leads us to designing a composite construction for multiwire actuators using a high compressive and flexural modulus material to support a softer container, still under way and not covered on this memory.

To attach Bowden tubing to the rest of the actuator's elements two U shaped components are used. These are 3D printed in ABS, which works on the edge of its temperature range, having its glass transition temperature at 105° C.

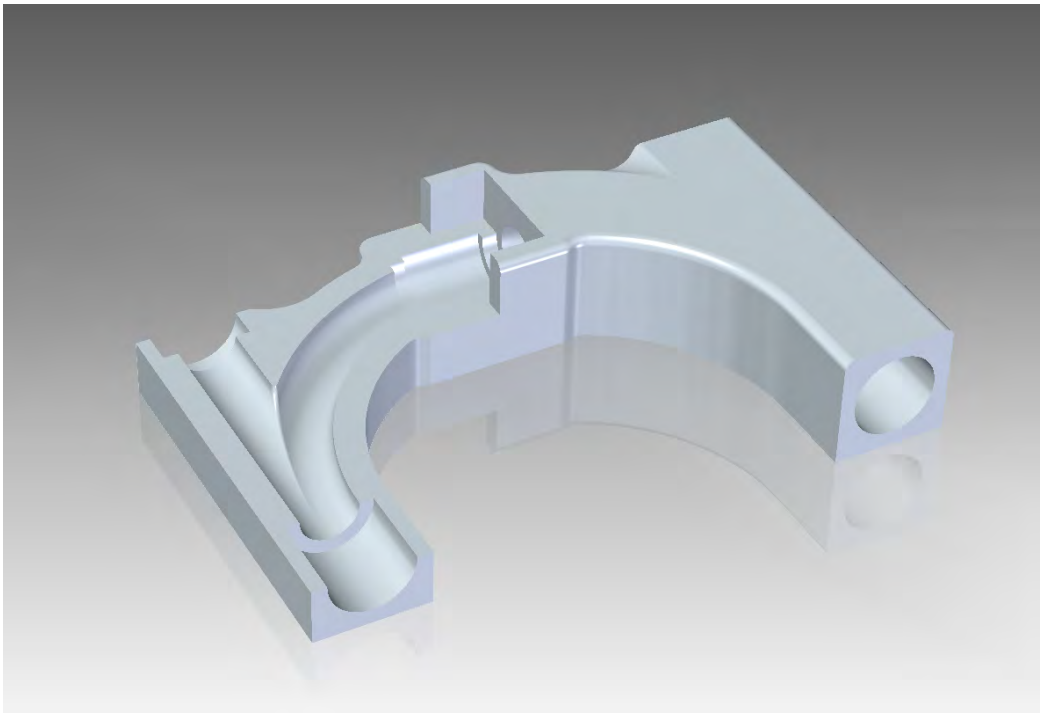

Figure 35: LT Junction Core extruded to show inner geometries

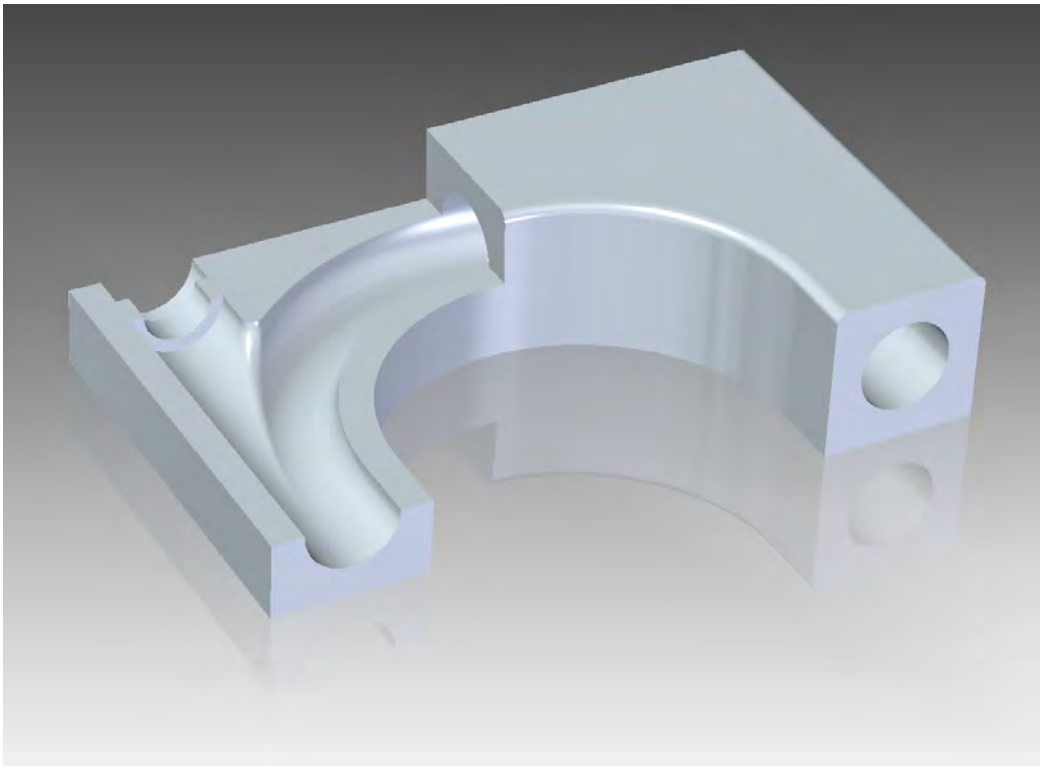

Figure 36: HT Junction Core extruded to show inner geometries

To give support to HT junction, a piece of curved PTFE tubing goes inside it. This piece was formed using an hot air stripper, packing smaller diameter high density plastic tubing inside and a mold, shown in Figure 37

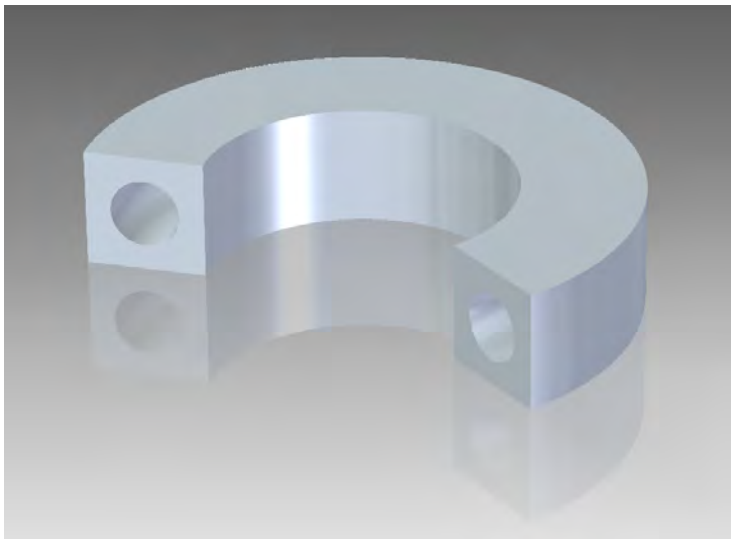

Figure 37: PTFE Tube Forming Mold

5.4.1 2D Heat Transfer Simulation

The two-dimensional heat transfer equation presented below needs to be solved numerically for our complex geometry.

$$\frac{\delta^2 T}{\delta x^2} + \frac{\delta^2 T}{\delta y^2} = 0 \tag{46}$$

We use a free CAD software to perform a simulation for our specific cross section, given the slender shape of the Bowden housing, a three dimensional approach would be redundant. Our geometry can be exactly matched, and initial conditions for HT chamber when the piston is moved towards LT end, having to heat up SMA wire and Bowden housing, are input. Equivalent power delivery is 120W, our expected heating element maximum. Simulation assumes thermal isolation to the surroundings.

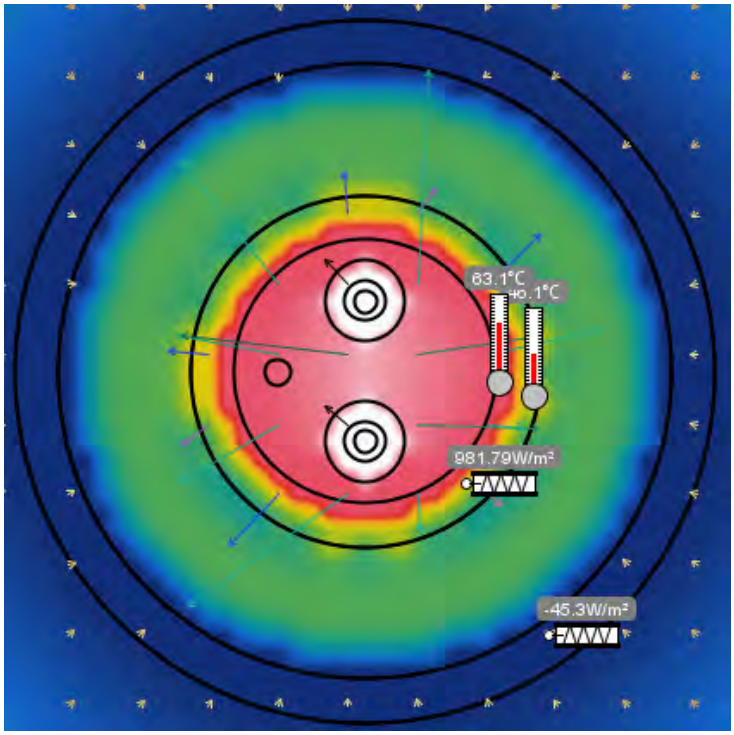

Figure 38: Cross Section Heat transfer Simulation

We are interested in Bowden's mean temperature versus time, we position temperature probes on its inner and outer walls and plot the data. On the visual interface we can see the heat propagating as a wave from the inner wall to the outer one, first from the fluid's stored energy, then as heat flow from the heating element. Outer wall reaches 70 ° in about 2.5s, when we can consider

terminal temperature is reached during normal operation, as power delivery won't be continuous.

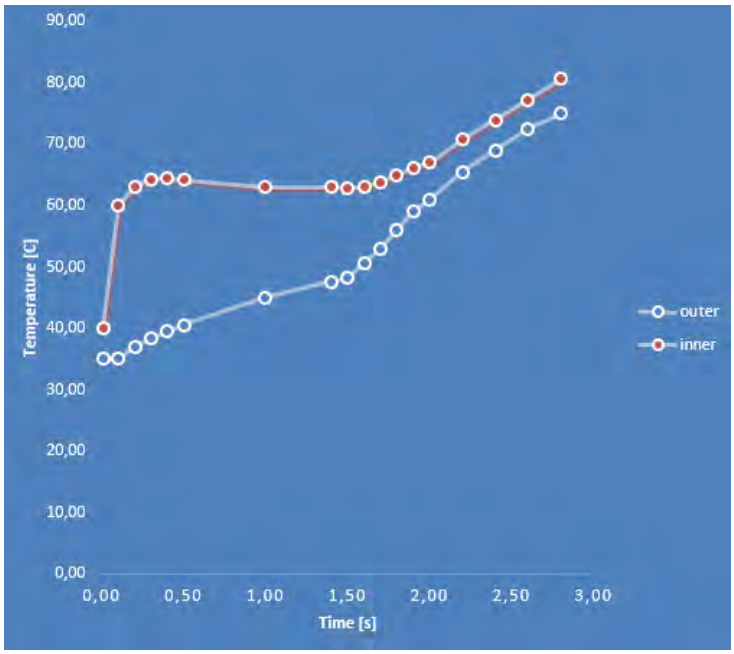

Figure 39: Bowden Housing Temperature over Time

Current Bowden tubing has a $RC = 31$ J /K, storing up to 1200 J during operation. Looking at Equation 3 what we want to reduce is, first wall thickness, then inner diameter. If Bowden Tubing and Water Container functionality are split between two components, a thin-walled low thermal capacitance tubing can be employed, such as PTFE or PET sleeving, with available geometries attaining a theoretical RC below 2. This would limit energy storage at 80 J, best case at 20 J. Changing to a lower VHC material like Carbon Fiber may provide a two-fold decrease in energy stored, but pultrusion manufacturing techniques, prevent ultra thin tubing feasibility.

For this topology to maintain energy efficiency this is probably the most troublesome aspect

5.5 Inner Tubing

On fluid flow requirements were established. Cheap industry solutions fit for these geometries can be polyamide pneumatic tubing ID 2,7 / ϵ 0.65 or PTFE wire sleeving ID 1,91 / ϵ 0.30 , ID 2,31 / ϵ 0.40 , ID 3,05 / ϵ 0,38.

Moment-curvature equation is stated as:

$$M = \frac{EI}{R} \tag{47}$$

where:

- E is Young modulus
- I is area moment of inertia
- R is curvature radius

Elastic strain energy stored from pure momentum, M, deformation in a bending beam or tubing is [28]:

$$U = \frac{1}{2}\theta M = \frac{\pi EI}{2R} \tag{48}$$

where θ is total angle, π on our setup

We are left with material selection and area moment of inertia optimization. From Equation 12 we can see how, even though any increase in inner diameter or wall thickness has great impact on its area moment of inertia, the fourth power element for wall thickness dominates. Added to PA almost 4 times bigger Young modulus, it is easy to see the best candidate. We can obtain reference values using Equation 48:

$$U = \frac{\pi EI}{2R} = \frac{\pi \cdot 0.5 \cdot 10^9 \cdot 1.295 \cdot 10^{-12}}{2 \cdot 0.05} = 0.020\text{J} \tag{49}$$

while for our worst case with PA, energy stored goes up to 0.626 J.

PA pneumatic tubing was chosen for its higher inner diameter and smaller fluid flow velocity differences between annular and inner tubing sections.

5.5.1 Water Inlet and Outlet

Trying to reduce the number of elements to be assembled and get the most out of each one, the belt link function, going from one piston to the other, was to be performed by the inner tubing.

Any belt link will always work in tension, either being pulled from one side or from the other. Longitudinal deformation of tubing can be divided in two components, the undrilled longer section and the drilled one, of there are two next to each piston. These holes allow for fluid flow in and out of the inner tubing. Designer has to optimize both their minor loss coefficient and their elongation tension. Three different hole placements are proposed using previous knowledge.

One hole most simple but also most mechanical structure weakening.

Two facing holes even with equivalent cross section to the one hole, it will probably worsen minor loss coefficient due to fluid flow constriction, but it spreads axial load more evenly.

Two offseted holes spreading holes will hopefully reduce its minor loss coefficient and also be less detrimental to mechanical structure.

Taking into account flow contraction, for 2.7 mm inner tubing cross section, 3.2 mm seems a good trade off.

We obtain two hole equivalent area with the following equation:

$$r_2 = \sqrt{\frac{1}{2}} \cdot r_1 = \sqrt{\frac{1}{2}} \cdot 3.2 = 2.26\text{mm} \tag{50}$$

Having three dimensional implications we resort to FEM for each hole topology. Linear static study with tetrahedral 0.36 mm element mesh was used for 20 N tension force. Holes at 10 mm from an end in a 50 mm long test piece, offsetted hole at 5mm axis distance. Adding length to the piece just extends simulation time without adding information, as the structural effects are local. Results are indeed symmetric from having one end fixed and pulling from the other and viceversa.

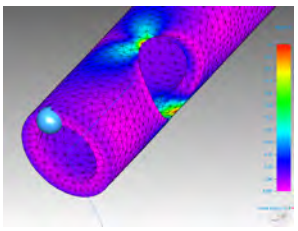

Figure 40: One hole FEA

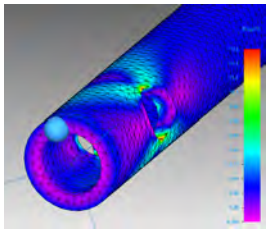

Figure 41: Two facing holes FEA

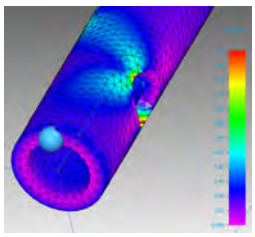

Figure 42: Two offsetted holes FEA

Table 5: Hole Placement FEA results

Type	Hole Diameter [mm]	Max. Strain	σ_max [MPa]
One hole	3.20	0.029	42.6
Two facing holes	2.26	0.009	13.3
Two offsetted holes	2.26	0.011	15.8

For selected PA tubing all topologies will stay in its elastic region, with its tensile strength at 80 MPa [29], but for a PTFE thin walled tubing we may have to resort to even bigger hole spread. Fluid flow performance is covered in Analysis chapter.

5.5.2 Sliding Flow Restrictor

An inner dynamic o-ring loosely compressed provides a enough pressure drop to completely restrict fluid flow. Its position on LT Junction is shown in Assembly chapter.

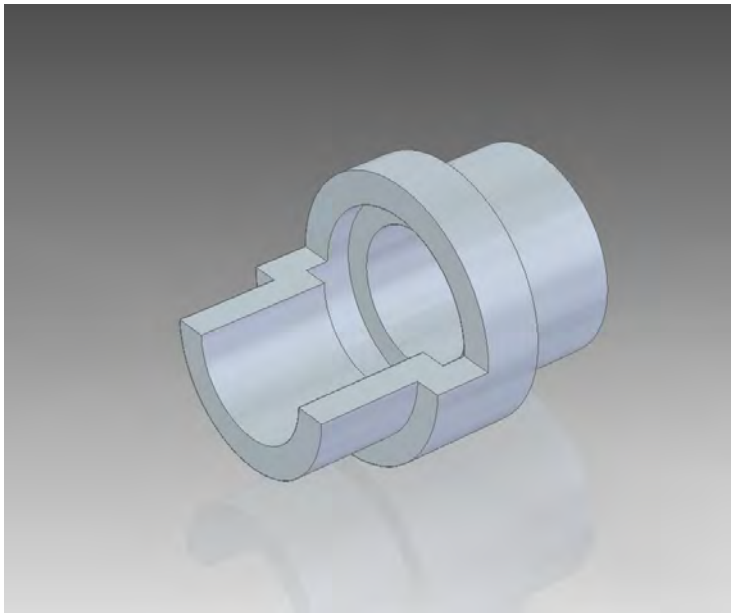

Figure 43: Sliding Flow Restrictor

5.6 Heating Element

A longitudinal heating element is needed for HT chamber that has to comply with the same governing equation for pure momentum deformation shown in Inner Tubing section. Two approaches are proposed.

First one is a continuous resistive wire that shares HT chamber with SMA wire to be actuated, entering from one end going up to the piston, performing a 180 ° turn at the piston, where it needs to slide, returning through the same path, carrying out another bigger radius 180 ° turn, reaching up to the piston for the third 180 ° and exiting the chamber.

These tight 180 ° turns inside Bowden tubing diameter pose a mechanical design challenge for both piston geometry and resistive wire. Maximum wire

diameter that can perform such turn without entering plastic region, supposing neutral axis is at the centre of the wire, is given by:

$$d = \frac{\sigma_y D}{E} \tag{51}$$

where:

- σ_y is yield tensile strength
- D is bend radius
- E is Young modulus

At the same time there are electrical requirements of resistance.

$$R = \rho \frac{L}{A} \tag{52}$$

where:

- ρ is resistivity
- L is length
- A is cross sectional area

resolving for its diameter:

$$d = \sqrt{\frac{4}{\pi} \rho \frac{L}{R}} \tag{53}$$

This gives us two equations the resistive wire diameter should comply with. To meet both targets multi strand wire is required, that enables us to increase effective cross section without increasing the wire diameter.

For mechanical requirements, common metallic compounds need to go down to micrometer thicknesses, which is not even considered on the American Wire Gauge wire thickness standard, with the smallest value, AWG40, being at 79 μm.
The only conductive material found that can achieve this performance is carbon fiber ribbon, composed by thousands of 7μm strands, and its high tensile strength and Young modulus,4.3 GPa and 240 GPa respectively [31], it easily stays in elastic region, with a maximum diameter in a 6mm Bowden tubing of 53μm.

Limitations to this material suitability come from, first, its high resistivity at 16 μmΩ, combined with a fixed L at 1m and targeting a resistance of 10Ω, that pushes the required effective diameter at 1.43 mm, second, the unavailability of a electrically insulating sleeve that can keep up with its mechanical performance.

An alternative solution is to use SMA wire's conductivity and the sliding needle interface to provide an electrical path for a resistive wire that travels between pistons, avoiding that those tight bends. Electrical and mechanical connection is done by using an helicoidal wrap as shown in Figure 44, kept together with high temperature glue and a heat shrink sleeving. As tension forces exerted on this mechanical bond are small it works reliably on this application.

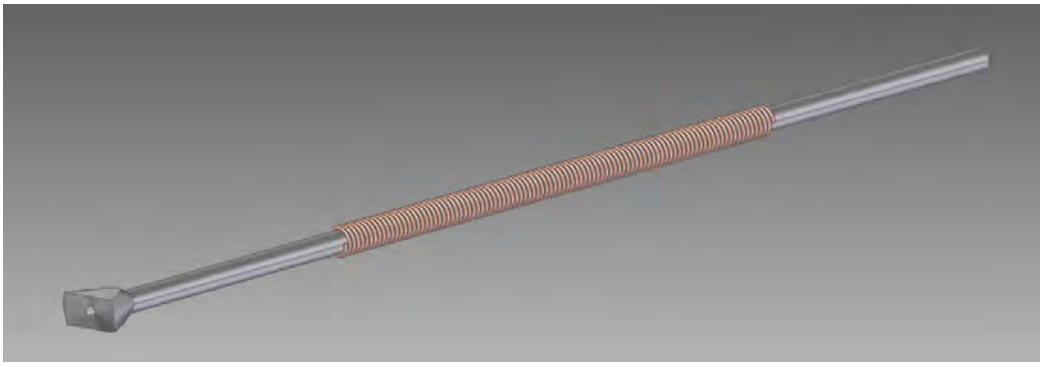

Figure 44: Helicoidal Copper Wire Wrapping

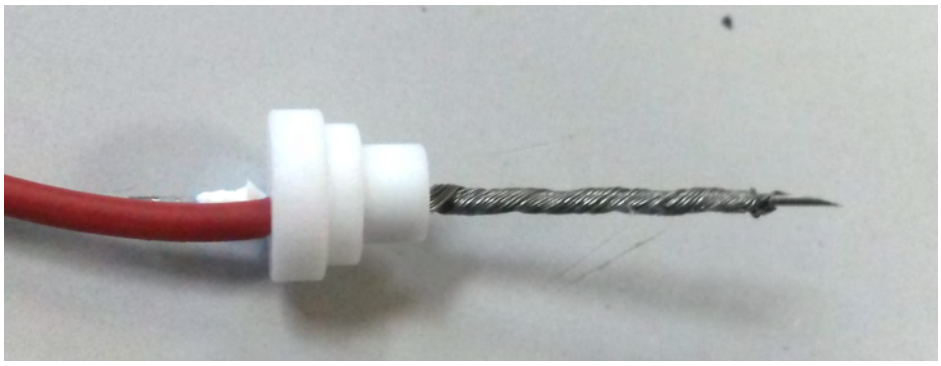

Figure 45: Partially Assembled HT End

From an electrical perspective we have an electrical diagram for each topology shown in Figure 46. For the continuous resistive wire topology we need a thermal bridge between resistive wire and electrical wire to reduce heat propagation through the high thermal conductivity heating wire. This is achieved by a 'necking' of the electrical wire, finding an equilibrium between its heat

generation and its electrical resistance. For the sliding heating element we have two variable SMA wire resistances that add up to a constant value for L = 0.5 m, and thermal bridge is provided by the needles.

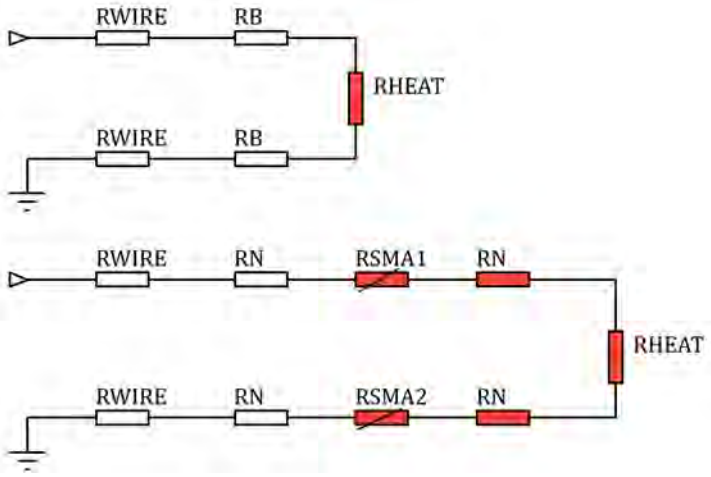

Figure 46: Electrical Heating Element Diagram

Regarding efficiency from an electrical point of view, first topology can go up to 98%, while second one is limited by the needle interfaces equivalent resistance, around 0.3 Ω, obtaining about 94% efficiency on the current setup.

$$d = \frac{R}{R + 2 \cdot R_N} = \frac{10}{10 + 4 \cdot 0.3} = 94.3\% \tag{54}$$

We set on the second topology due to feasibility concerns of the first one.

5.7 Round Belt, Pulley and Electric Motor

For piston actuation a round belt mechanical transmission system was devised, as depicted on Figure 21. On Inner Tubing chapter the LT chamber side of the belt was covered. For HT chamber, we need a way to pull from each piston that, can go in and out of the fluid container, use the existing air-liquid interface, can sustain a tension strength around 25 MPa, 90 ° is in its temperature range (may get in touch with heating element), and has reduced volumetric heat capacity for minimal heat loss.

Plastic monofilament wire, commonly used as fishing line, positioned itself as a superior candidate. Although PA6 has a low VHC, its high water absorption rates at high temperatures [32] may present issues for the liquid-air interface devised. PVDF, also known as fluorocarbon, even though it has higher VHC value, comparable to that of PTFE as both are fluoropolymers, has

extremely low water absorption, has a yield tensile strength rating at 45 MPa, and its tensile Young modulus around 15 GPa, limits worst case elongation to 15 mm. [33].

A tensioned pulley mechanical transmission force governing equation [30]is:

$$F_1 = e^{\mu\theta} \cdot F_2 \tag{55}$$

where:

- F_1 is pulling force on tight wire
- F_2 is pulling force on slack wire
- e is Euler number
- μ is pulley friction coefficient
- θ is angle of wire resting on pulley

Reading from the equation we see that the higher slack wire's pulling force is, the more force can be transmitted, meaning a good pre-tensioning and low elasticity are preferred. The exponentially related components can also be tuned, pulley friction can be improved by wrapping the U-shaped pulley profile in high-friction rubber tape, while angle can be increased by constraining the wire's path adding secondary wheels, for simplicity's sake we will have just a 180 ° angle.

It could happen that if actuation force is higher that F_1, the wire will just slide over the pulley when it turns. At this step we will just avoid this by increasing pre-tensioning force.

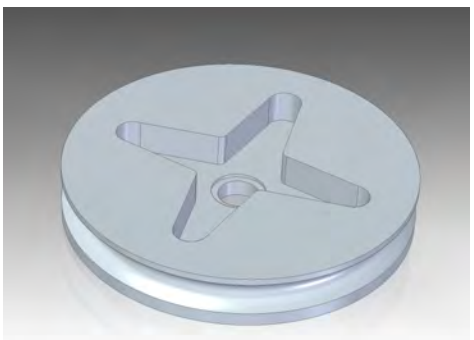

Figure 47: U-profile Pulley fit for a MG995 servomotor

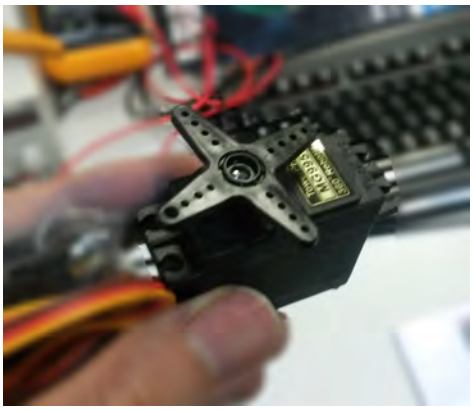

Figure 48: MG995 Servomotor

To actuate our pulley we require an electric motor, that allows for controllability of pulley's position and speed. A DC servomotor is used as an initial prototyping solution, providing a tight package for motor, gearing and controller.

Cheap DC servomotor are characterized by their stall torque and no load speed, given for a 60 ° turn, at 4.8V and 6V. These presentation, although usually useful for comparison may be deceiving for the designer, hoping that listed torque is achieved at listed speed. The equation solved for speed would look like this:

$$v = v_{max} \cdot \left(1 - \frac{T}{T_{max}}\right) \tag{56}$$

where:

- v_{max} is no load speed
- T_{max} is stall torque
- T is current torque

If speed is presented on rpm on continuous rotation, which our servos have to be enabled for, as they will usually have mechanically limited rotation angle, we can obtain torque-speed curves for different servos, presented on Figure 49.

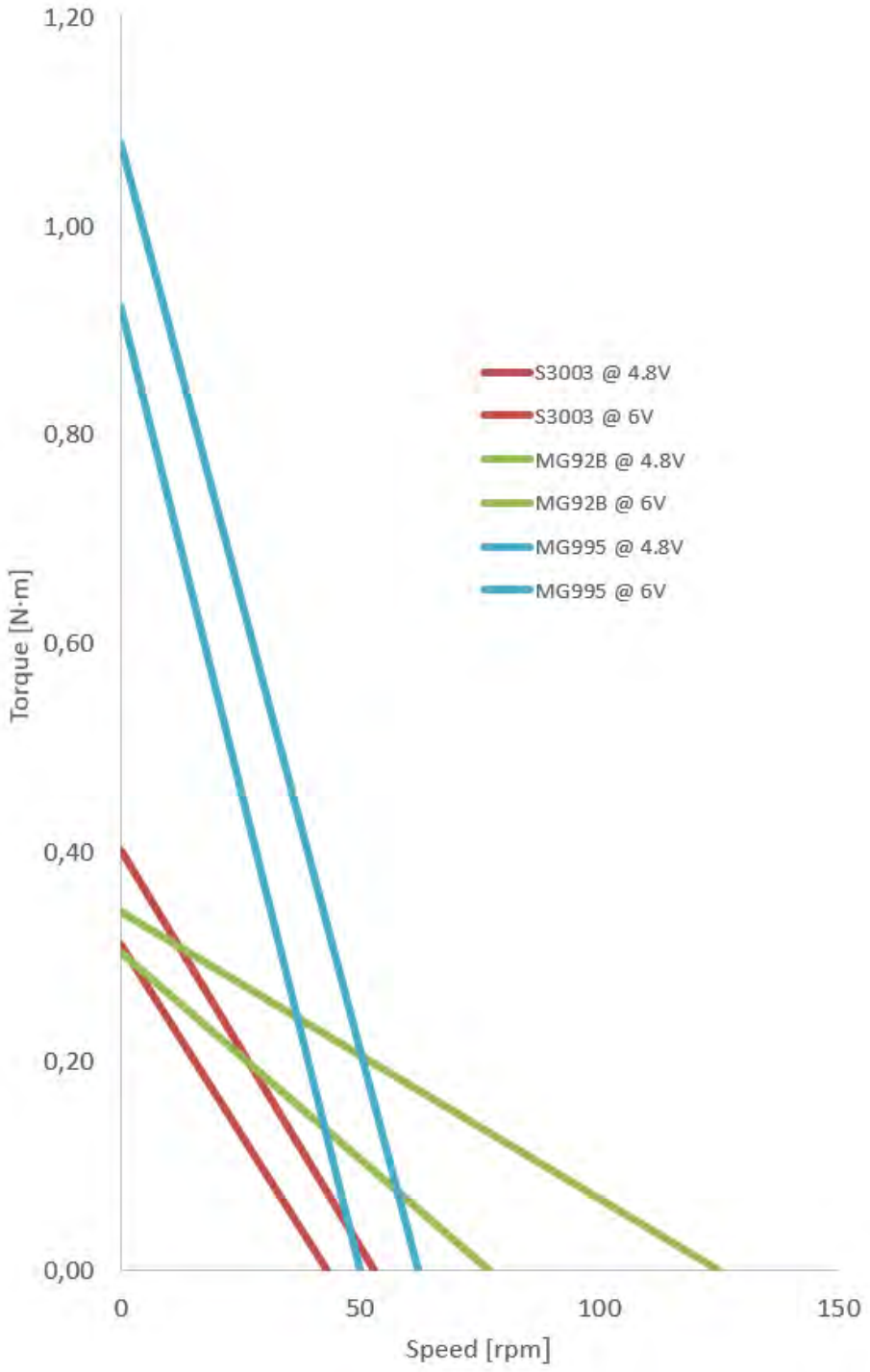

Figure 49: Servomotor Torque-Speed Comparison

Behind these curves there are other parameters such as weight, usually being proportional to torque, controller architecture, either digital or analog,

the first having faster update rates, the second consuming less energy on idle, and energy efficiency, that for DC motors ideally behaves as shown on Figure 50 normalized, where efficiency is output power over current times fixed voltage. It's easy to understand how heat generation when operating at a torque to the right of its maximum power torque can quickly damage the motor.

Apart from commercially available servomotor selection, we can optimize motor operation by changing our pulley diameter, that will allow to meet piston speed requirements, fixed at five second for half an actuation cycle, $v_{target} = 0.1$ m/s for $L = 0.5$m Each servo motor will have a different optimal pulley diameter.

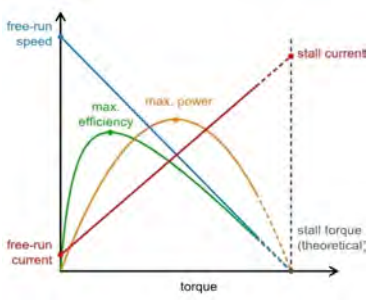

Figure 50: Servomotor Torque-Speed Comparison [34]

Plotting T_{max} against v_{max} against pulley diameter, at fixed target speed and for an actuation force of 12 N, which we augment by a safety factor of 2, which is an estimation of belt actuation force. Range for each value introduced from Figure 50 we obtain a 3D curve that allows for visual optimization of pulley diameter:

$$T_{max} = \frac{2 \cdot F \cdot \frac{D}{2}}{1 - \frac{v_{target}}{v_{max}}} \tag{57}$$

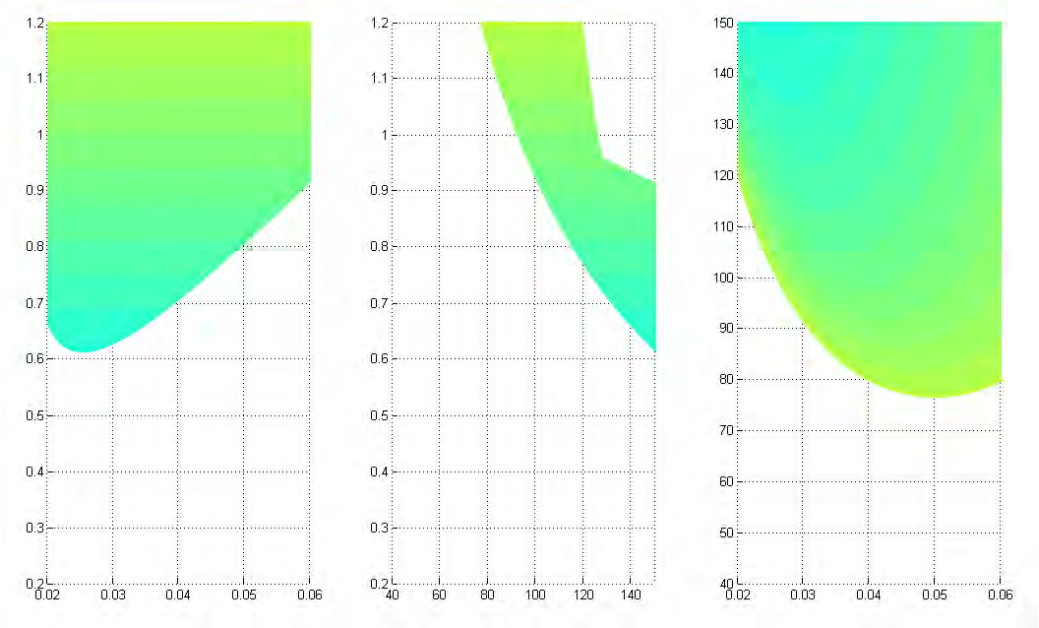

Figure 51: Torque Speed Pulley Diameter Plane. From left to right: Torque-Diameter, Torque-Speed, Speed-Diameter in N·m, rpm and m respectively

All the empty space on the central graph signifies how high torque and speed requirements quickly rule out most of these cheap servos. We went for a 50 mm pulley on a MG995 servomotor, for its maximum speed, while slightly losing some torque capability. Servo control is covered on Rapid Control Prototyping chapter.

This servomotor holder can be slid and fixed on two parallel rails using two cup square bolts, allowing for belt pre-tensioning. Attached to these rails are two framing squares in parallel, on which HT Junction rests, allowing for vertical displacement to avoid shearing forces on SMA wires and motion wire when exiting or entering the needles.

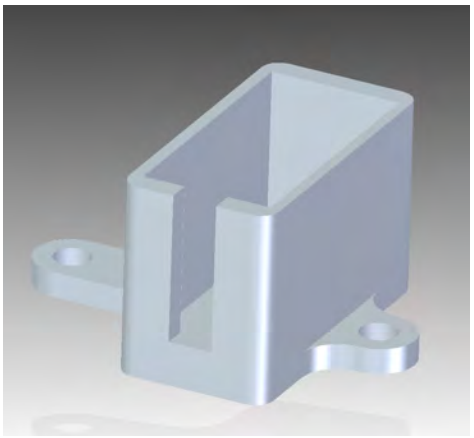

Figure 52: Servomotor Holder that enables belt pre-tensioning

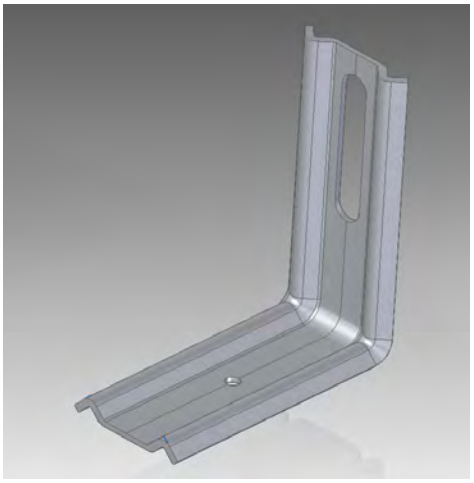

Figure 53: HT Junction Support

5.8 Pump and Radiator

Pump selection is mostly ruled by scarce commercial availability for our application, wanting high volumetric flow rate, low weight and volume and high efficiency. TCS Micropumps offers a range of suitable products in this category.

M100S micropump up can inject up to to 6.7 ml/s volumetric flor rate, with a listed power consumption around 1 W, all listed parameters spot on as tested. The only shortcoming for the purchased pump is not being self-priming, which is also offered on M100S' submersible version, most useful when doing miscellaneous testing.

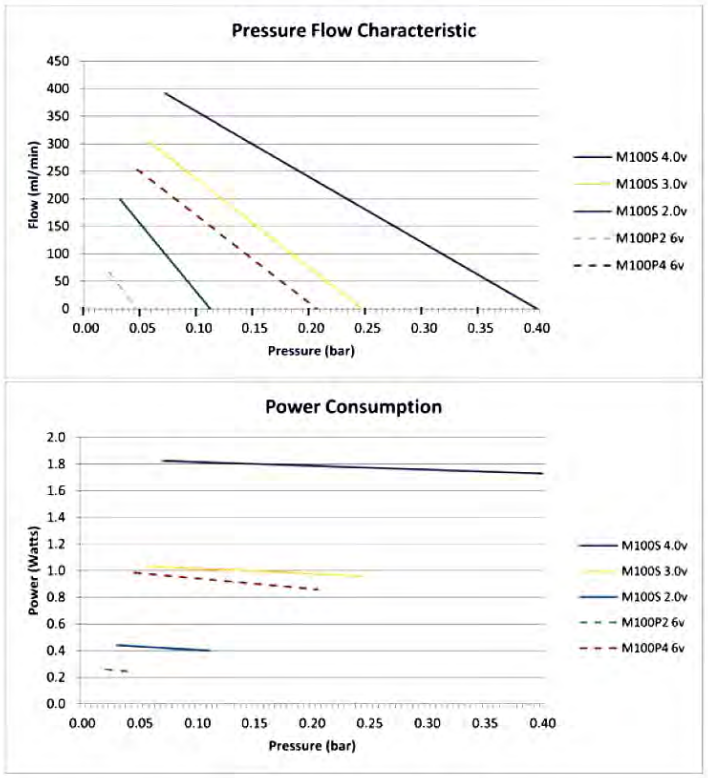

Figure 54: Pump Performance Graphs

Given the time investment required for an application specific radiator design, that would be tailored to both our flow speed and pressure drop targets, while optimizing stringent W/kg and W/m^2 figures, we decided to postpone this part of the design.

Preliminary research analysis points at conductive foams made out of silicon carbide [35] or aluminium [36], traversed by LT chamber heat-transfer fluid, to bring equivalent thermal resistance as close to zero as possible.

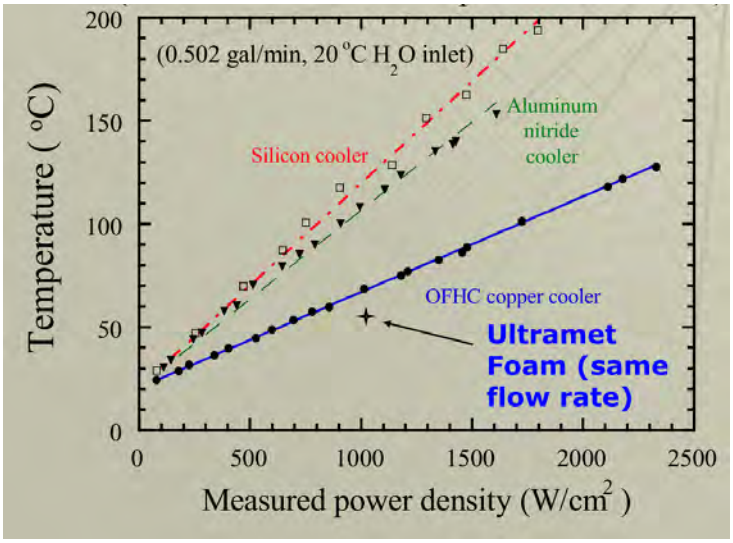

Figure 55: Heat Exchanger Comparison

Its function will be performed by a vertical water container, where water a few degrees under ambient temperature will be provided during its operation. Its relative high volume to the one present inside the actuator and strategic positioning of inlet and outlet ports allows for some natural convection to take advantage of.

5.9 Flexible Dewar Vase

To reduce energy loss from LT chamber, heat flow can be restricted implementing a Dewar vase inspired vacuum jacket around the actuator. Maintaining air as our fluid , we need to reduce its pressure to augment its mean free path versus the characteristic length, given by dimensionless Knudsen number. An approximation to the behaviour seen at reduced pressure is graphed at Figure **??** found at [39], from Equation 58 we can obtain our reduced pressure target, expected to be around 0.35 Pa.

$$P = \frac{PP \cdot T}{L} \tag{58}$$

where:

- PP is pressure parameter
- T is temperature
- L is characteristic length

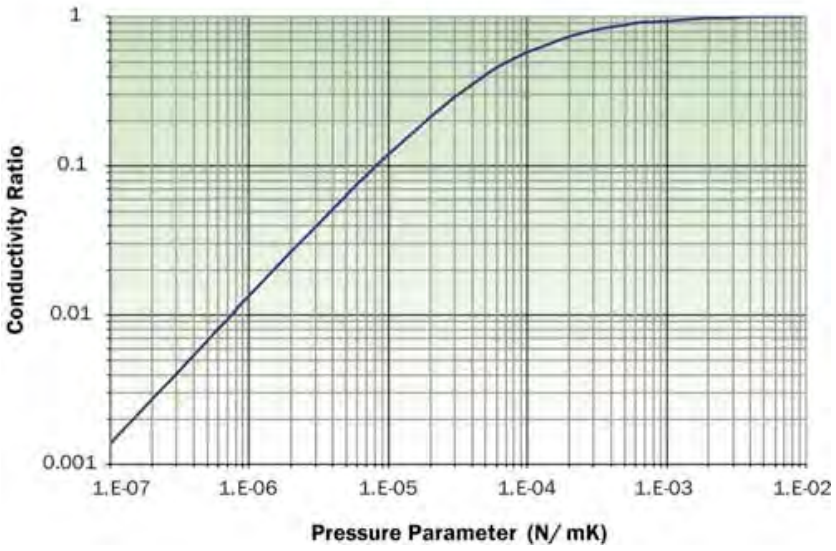

Figure 56: Thermal Conductivity at Reduced Air Pressure

Creating a medium vacuum in a jacket that surrounds our actuator while retaining its flexibility may be achieved through already available pneumatic industry polyamide circular tubing conformed to shape. The ability of this tubing to maintain its structural integrity for the particular geometry of the chamber at a pressure difference close to 1 bar has to be tested. 3-dimensional complexity points at FEA as the right tool for this task.

For this test two different wall thicknesses are tested at standard conditions regarding temperature and surrounding pressures. A linear static study is performed with a tetrahedral mesh of 6mm, test piece's length is 500mm, diameter 10 mm, widest distance 20 mm, enough to surround two Bowden tubes side by side.

This is by no means a proof of concept, and it was not empirically tested, but it states that feasibility of such concept may be at hand, as long as air tightness is achieved, allowing for HT chamber dissipation losses to be limited.

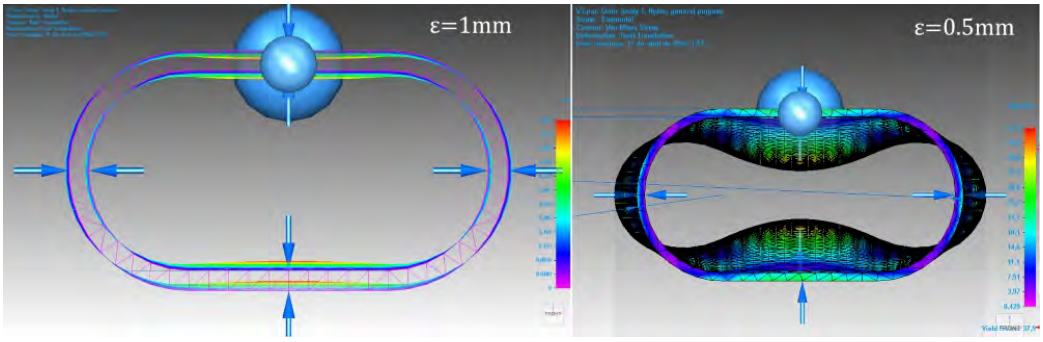

Figure 57: Wall Deflection for Medium Vacuum Vessel of PA6

6 Electronic and Control Design

6.1 Rapid Control Prototyping

Thanks to previously developed software modules, Simulink real-time modules can be ported to operate as standalone from a microcontroller. We use STM32F4DISCOVERY Discovery kit cards with a STM32F407VGT6 at its core, surrounded by the most commonly used peripherals, like those below..

The different modules used and its functionality are:

PWM Module (2x) as output for:

- Servomotor control
- Heating Element

ADC Module (4x) as input for:

- Thermistors

DAC Module (1x) as output for:

- Pump

SSI Interface Module (1x) as input for:

- Hall Effect Sensor

USB IN and USB OUT (1x) for real time control and data logging

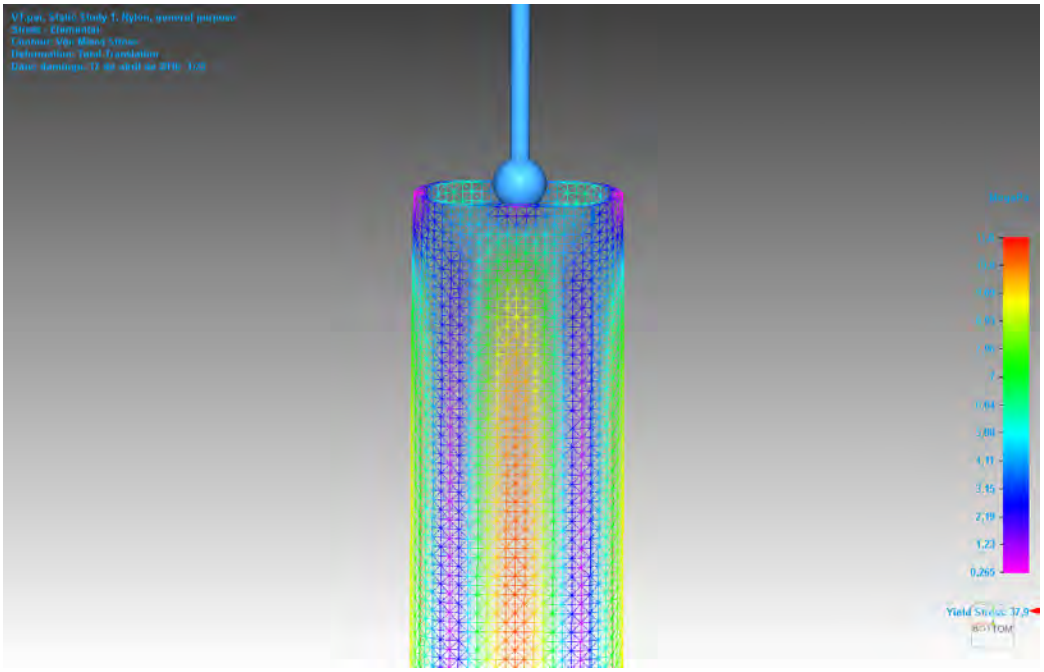

Figure 58: Stress Distribution for Medium Vacuum Vessel of PA6

6.1.1 Motor Control

A digital continuous rotation servo needs an specific control signal pattern for precise position control shown below following a sinusoidal on open loop. The loop will be closed with a hall effect sensor measuring SMA wire displacement.

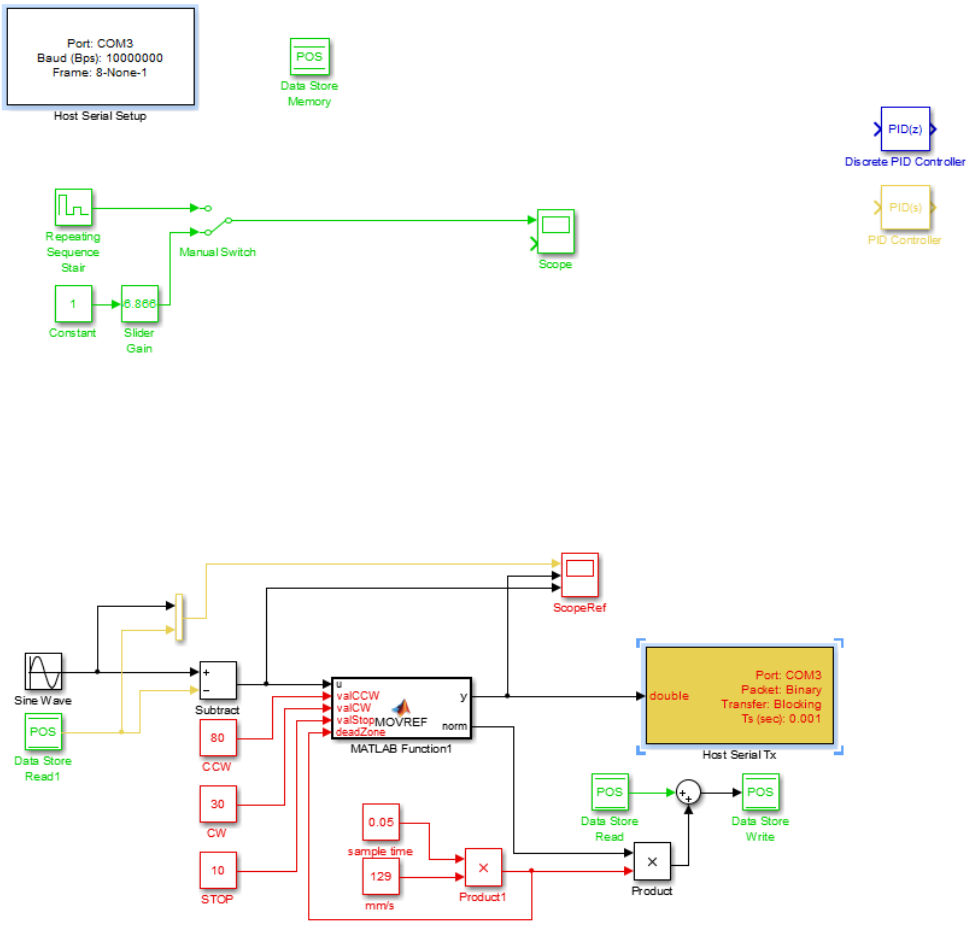

Figure 59: Simulink Motor Control Scheme

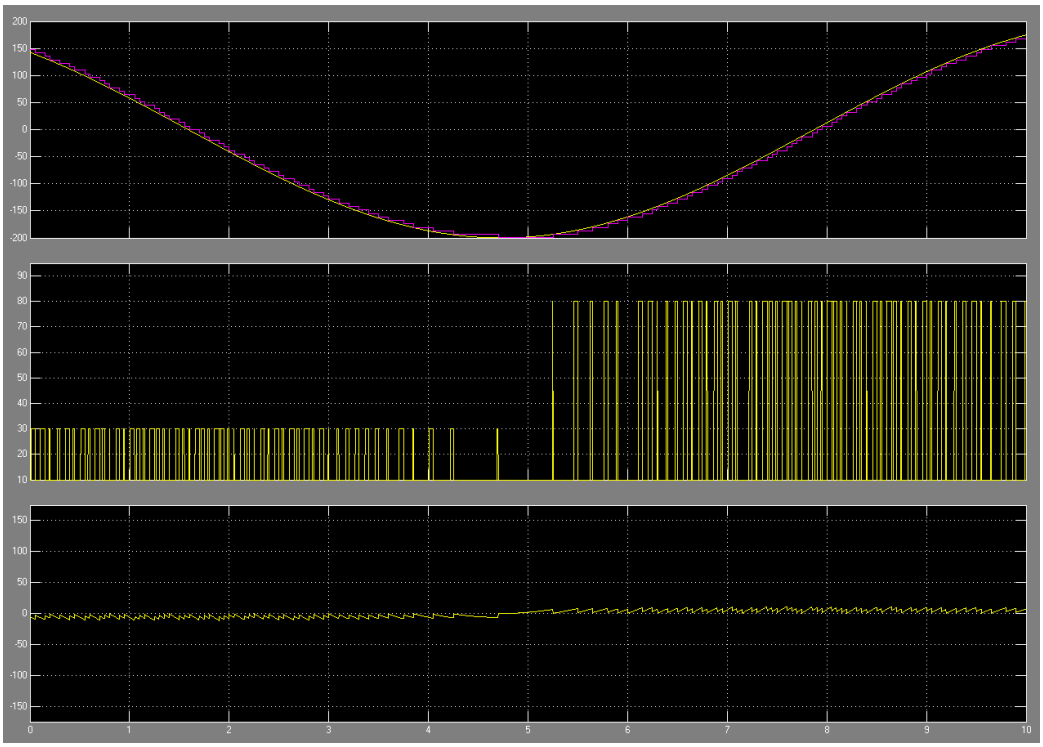

Figure 60: Simulink Motor Control Scope

6.2 Thermistor Polarization

For pump and heating element control we need temperature references across the actuator. Thermistors, although highly nonlinear can easily be interfaced with a microcontroller's 12bit ADC by a simple voltage divider, assuring maximum power dissipation figure is met at all times.

Having V_{CC} fixed at 5V and knowing the operating temperature range on each chamber, from manufacturer data values [40] we can select R_{NTC} nominal values whose minimum value will be kept in the over 5kΩ range to limit current, reducing power consumption. HT chamber NTC will be 100kΩ and LT chamber 10 kΩ.

Table 6: NTC Resistance Values

	T_{min}	R_{max}	T_{max}	R_{min}
LT Chamber	20	12.1 kΩ	40	5.7 kΩ
HT Chamber	70	24.1 kΩ	85	10.1 kΩ

An approximation from Steinhart-Hart equation for resistance variation with temperature is:

$$R_{NTC} = R_0 \cdot e^{-\beta\left(\frac{1}{T_0}-\frac{1}{T}\right)} \tag{59}$$

where:

- R_0 is resistance value at calibration temperature
- β is characteristic parameter
- T_0 is calibration temperature, usually 25° C

Error from this approximation is around 0.3 °C around ambient temperature, and up to 1 °C at 80°C, which at this stage is deemed good enough.

Given the large variations in R_{NTC} value we cannot use small signal analysis for optimizing R. Voltage variation expression is:

$$\Delta V = V_{CC}\left(\frac{R_{max}}{R+R_{max}} - \frac{R_{min}}{R+R_{min}}\right) \tag{60}$$

where:

- R_{max} is highest value on its operating temperature range
- R_{min} is smallest value on its operating temperature range

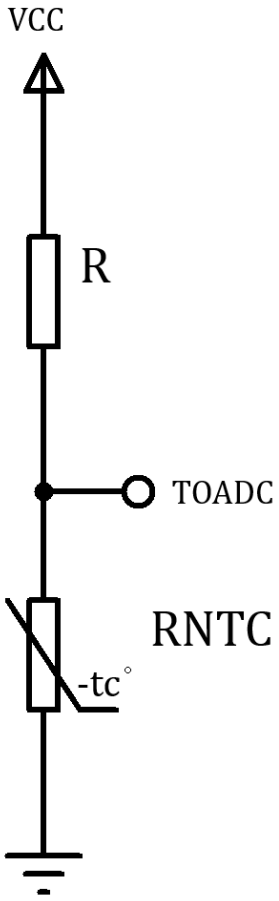

Figure 61: Thermistor Polarization Circuit

Solving $\frac{d\Delta V}{dR} = 0$ we can maximize ΔV value, obtaining:

$$R = \sqrt{R_{max} \cdot R_{min}} \tag{61}$$

Applying to Table 6 values, LT chamber obtains 8.3 kΩ, HT chamber 15.6 kΩ, 8.2 kΩ, 16 kΩ on commercial 5% tolerance values. If we just used target temperature for each chamber, the resistance value at the given temperature would be optimal our R.

Maximum power dissipation comes with lowest resistance value, having the start-up operating range covered, with manufacturer absolute rating at 18 mW:

$$P_{NTC} = \frac{V_{CC}^2 \cdot R_{min}}{(R+R_{min}^2)^2} \tag{62}$$

Table 7: NTC Highest Power Dissipation

	R_{min}	P_{max}
LT Chamber	5.7 kΩ	0.72 mW
HT Chamber	10.1 kΩ	0.38 mW

Equations to obtain resistance and temperature from the measured voltage, V_m, are:

$$R_{NTC} = \frac{V_m \cdot R}{V_{CC} - V_m} \tag{63}$$

$$T° = \frac{1}{\frac{1}{T_0} - \frac{1}{\beta} \ln \frac{R_{NTC}}{R_0}} \tag{64}$$

With a 12bit ADC, the voltage resolution step should be 1.22 mV, obtaining almost 900 steps on the operating temperature range. Sensitivity will be mostly limited by Steinhart-Hart approximation equation.

6.3 Pump Control

Knowing actuator MTBF figure may come from its pump, stress from hard switching circuits is avoided by using a MOSFET in series as an ohmic load. R_{SENSE} should provide a high enough reference voltage to be in range of STM32F4 DAC capabilities. This open loop control

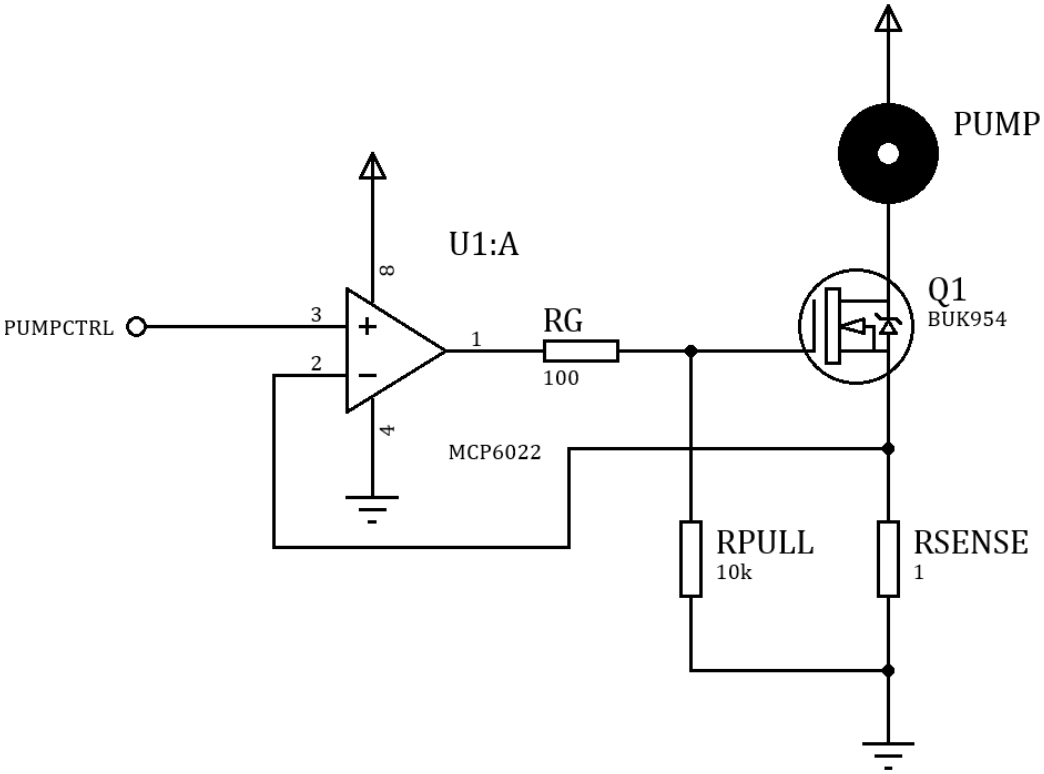

Figure 62: Pump Control Diagram

6.4 PCB Design

A PCB was designed for electronic element integration. Featuring two layers and high power rails.

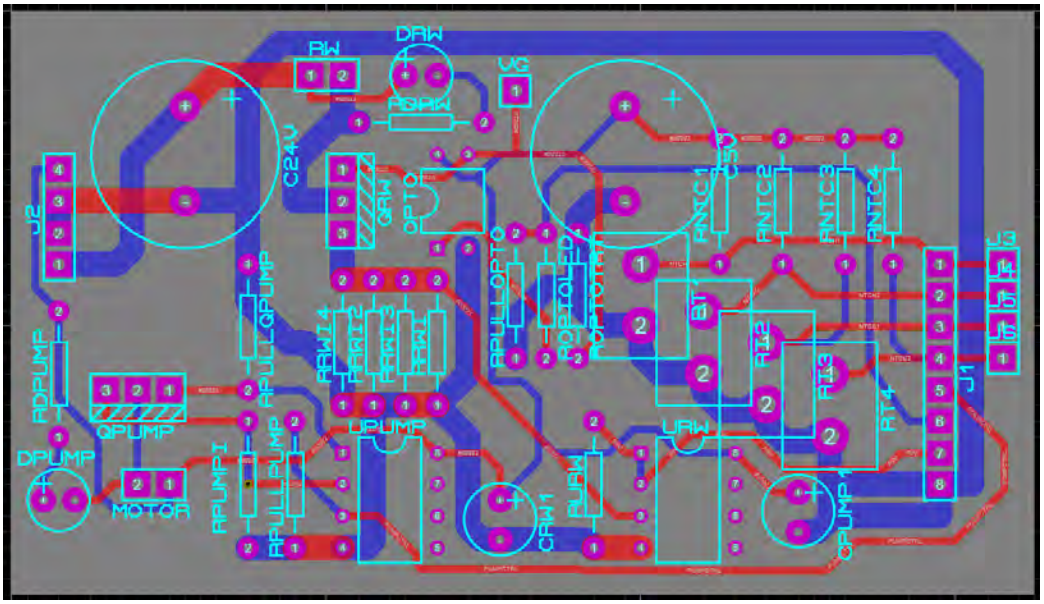

Figure 63: PCB Rounting

7 Implementation Analysis

7.1 Piston Actuation Force

Piston actuation is probably the most complex aspect of this topology. Friction force and speed establish efficiency and actuation time for the actuator.

As explained on Liquid-Liquid Interface chapter, HNBR o-ring's compression set optimization was done empirically. Test setup included a 20 N linear dynamometer, our PTFE Bowden tubing and the various piston as show on Figure 64. The Bowden tubing was manually slid over the piston, distance between the piston and the dynamometer being fixed by the cable, over a premeasured distance, maintaining a constant pulling force on the dynamometer scale, while also measuring time. Water was added as its hydrodynamic properties reduced actuation, getting a more relevant result to what will be seen on the implementation.

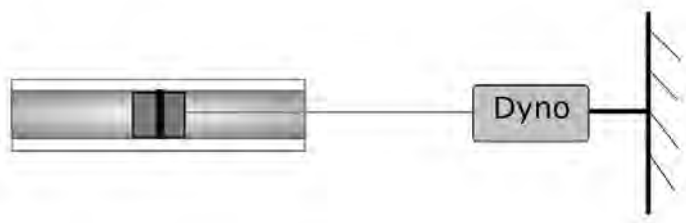

Figure 64: Piston Friction Test

The measurement uncertainty of this kind of setup is high, but averaging multiple measurements, up to 5 times, allowed for a reliable way of comparing test pieces, as can be seen of Figure 65. These curves can be fitted with an inverse exponential equation $t = a \cdot e^{-b \cdot F}$, a in the order of hundreds, b between 0.5 and 0.9, relevant for control strategies. From the legend, curves indicating 'w/o' refer to not having applied grease to them. Lubrication was only performed in the highest compression sets, as travel time quickly fell below our measuring capabilities, which was great news. Work performed was also plotted versus force.

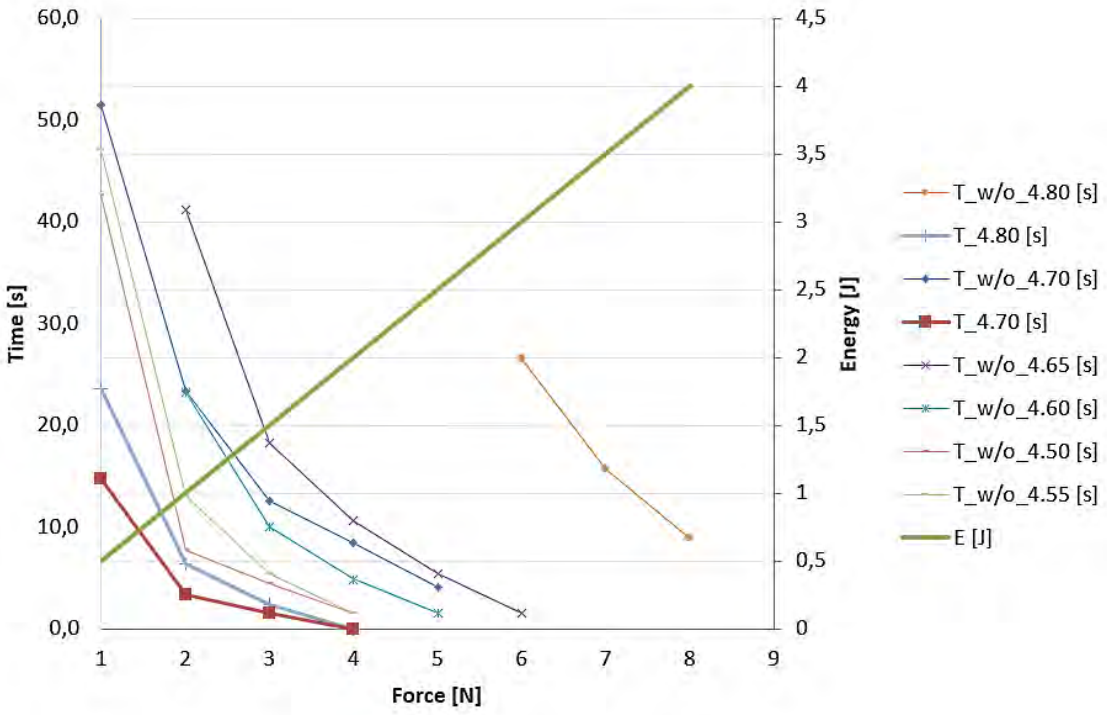

Figure 65: Piston Friction Force-Time Graph for $L = 0.5$m

This test was also done to the sliding flow restrictor, obtaining a maximum reading of 1 N for any pulling force. For this component it was noticed how for a NBR o-ring and PA inner tubing, sticking phenomena cannot be disregarded, presenting a characterization below of its evolution over time. Swapping to a less porous o-ring material like FKM, or a PTFE inner tubing would get rid of this event altogether.

Table 8: Sticking Characterization

t [s]	0	20	50	100	200	300	500	1440
F [N]	0.25	0.5	0.5	1	1.15	1.5	1.5	3

The compounded actuation force across the motion wire can be seen as a lumped model of :

- Air-liquid interface needle friction
- Piston O-ring friction
- Flow restrictor O-ring friction
- Inner tubing friction and elastic energy exchange due to curvature

shown below, that can be related to the belt equations shown in Round Belt chapter. When motion wire enters and exits parallel to a needle, maximum reading was 1 N, tested as metioned before.

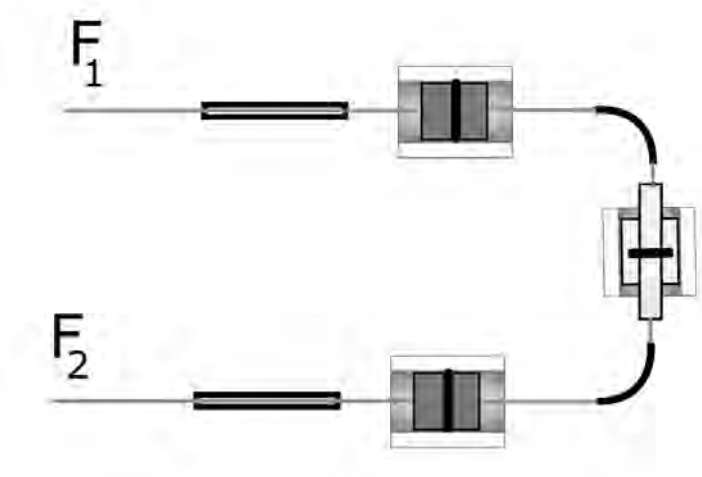

Figure 66: Belt Friction Distribution

Maximum total friction is expected to be at 12 J after all previous testing.

7.2 Watertightness

Watertightness between chambers is key for thermal efficiency, as any liquid going from one chamber to the other implies great advection losses, ruled by Equation 5.

A testing method was devised for reliably estimating fluid exchange between chambers using a pH meter and different pH fluids. Using molar concentration equilibrium for a molecule, and given complete dissociation the equation for the amount of volume that goes through the piston is:

$$x_1 = V_1 \cdot \frac{C_1' - C_1}{C_2 - C_1} = V_1 \cdot \frac{10^{-\mathrm{pH}_1'} - 10^{-\mathrm{pH}_1}}{10^{-\mathrm{pH}_2} - 10^{-\mathrm{pH}_1}} \tag{65}$$

where:

- V_1 is initial volume
- C_1' is final concentration on side 1
- C_1 is initial concentration on side 1
- C_2 is initial concentration on side 2

$$pH = -\log[H^+] \tag{66}$$

where H^+ is hydrogen ion concentration

Thanks to the logarithmic relationship and the ph meter resolution, having a pH 4 and a ph 10 liquid and using 1 ml as testing sample, the resolution can be as low as 23 μl, which is remarkable. For a worst case scenario, using the 4.60 groove diameter test piece and performing 100 full actuations of 34 cm each, a pH value of 4.19 was measured, indicating 354 μl transfer, averaging 3.54 μl per actuation, representing a loss of 0.59 ± 0.01 J.

Figure 67: Watertightness O-ring Testing

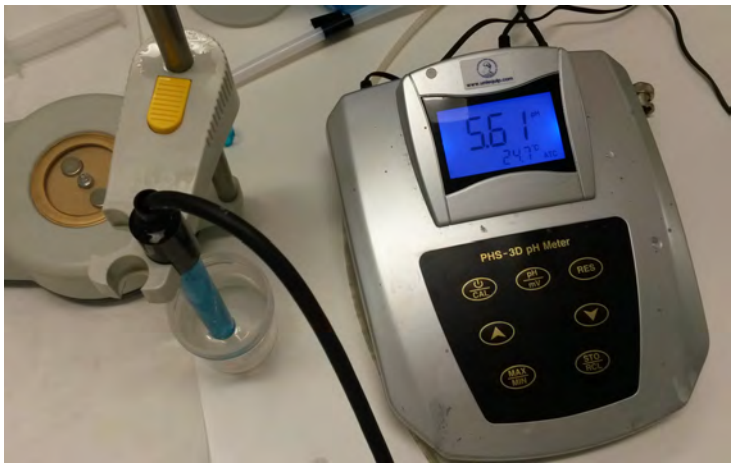

Figure 68: pH meter measurement

Watertightness on LT junction to Bowden and HT junction to Bowden was a mess, as was more or less expected. Adding a threaded ring that clips Bowden Tubing in place would easily solve this.

Watertightness on sliding flow restrictor was complete.

7.3 Dissipative Losses

To explain interest on a vacuum jacket, a theoretical estimation of convection and radiation heat flow if no vacuum jacket is used for HT chamber was obtained from cylindrical unidirectional equations for our Bowden sheath.

$$q_{conv} = \frac{\Delta T}{\left(\frac{\ln \frac{r_e}{r_i}}{2\pi L k_{PTFE}} + \frac{1}{2\pi r_e L h_{BWD}} \right)} \tag{67}$$

where:

- k_{PTFE} is PTFE thermal conductivity, 0.24 W/mK
- h_{BWD} is natural convection coefficient

$$q_{rad} = \epsilon\sigma\left(T_{BWD}^4 - T_{amb}^4 \right) \cdot 2\pi r_e L \tag{68}$$

where:

- ϵ is PTFE emissivity, 0.84
- σ is Stefan–Boltzmann constant

Ambient temperature is a driving factor for these values so heat flows are plotted against it. Given the interaction between convection and radiation, a iterative method was used to converge to the solution. From empirical data, natural convection coefficient is taken at 20 W / m^2K .

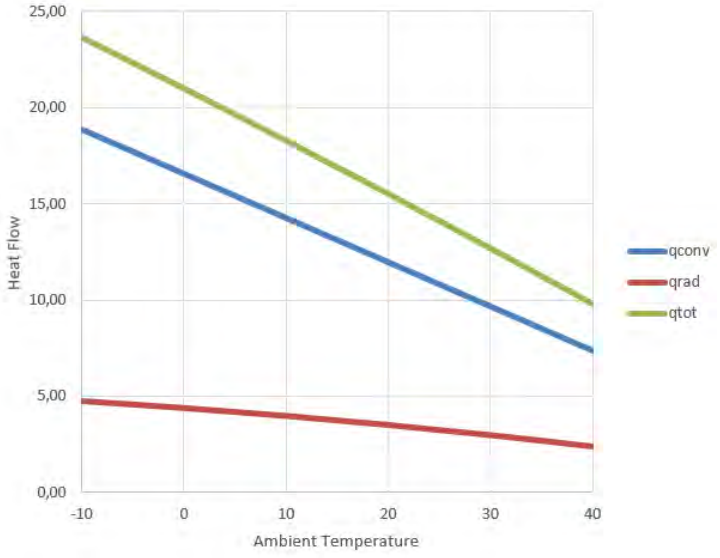

Figure 69: Assembled LT Chamber Juntion

Shown behaviour would also affect radiator performance, pointing at a Peltier module to increase temperature delta for an outdoors solution.

7.4 Fluid Flow Losses

Combining pump pressure flow curve and a graduated cylinder we can obtain pressure drop in a water line.

The method consists in setting the pump's input voltage at 2, 3 and 4V to use manufacturer curves, and pump a 200 ml volume of water, measured by a graduated cylinder, while measuring time employed. Dividing this terms results in a volumetric flow rate. The higher the value the better, as it requires less input power to inject a certain flow rate.

Fluid path is shown in Figure 70. On such a setup, we will have both major and minor losses, for the different inner tubing hole topologies, the first ones will remain constant while the second ones change.

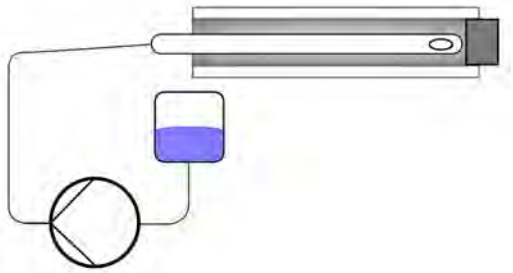

Figure 70: Pressure Drop Test

Plotting the results we find the expected performance, as the bigger diameter hole provide less flow constriction, while the dual hole setups fall behind. There is remarkable difference between facing and offsetted holes, indicating turbulent phenomena wreaking havoc. Also interesting is the non linear dependence between flow rate and power consumption, relevant for optimal control.

From the actuator's fluid path perspective, as the length of the inner and outer tubes already matches the implemented ones, the only elements missing from the line are the contraction and the inner tube curvature. From the difference between the theoretical major loss and the empirical measurements, we can expect the pump to be well into operating region.

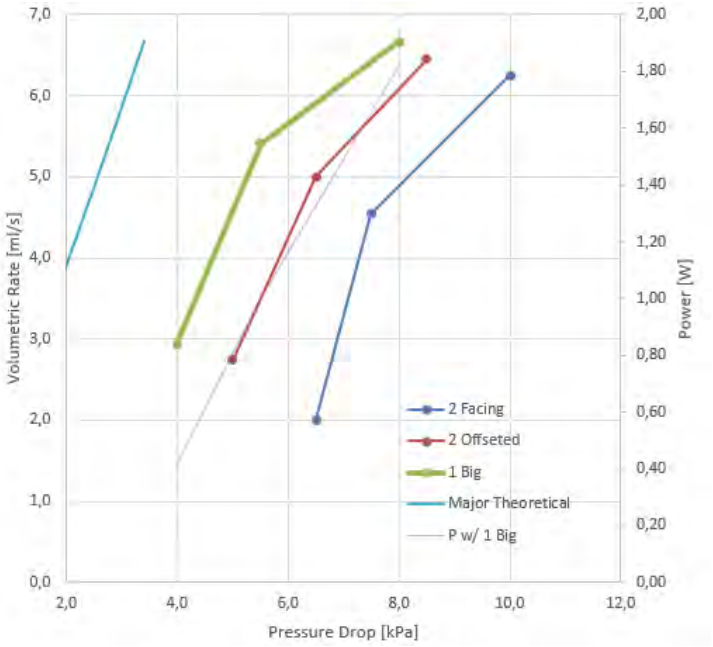

Figure 71: Pressure Drop Test

7.5 Assembly and Weight

Definitely one of the deficits of this topology is its assembly complexity, although it was manageable, there is a lot of room for improvement employing design for assembly methodologies.

From a preliminary assembly, trying to test the complete to acquire further knowledge, although not an objective for this work, we learned power delivery to the heating element worked flawlessly, but actuation force was above 30 N, rendering current assembly non operational. Thanks to all the previous analysis it indicates some misshape on some of the last-minute solutions used during assembly, that will be fixed in the future.

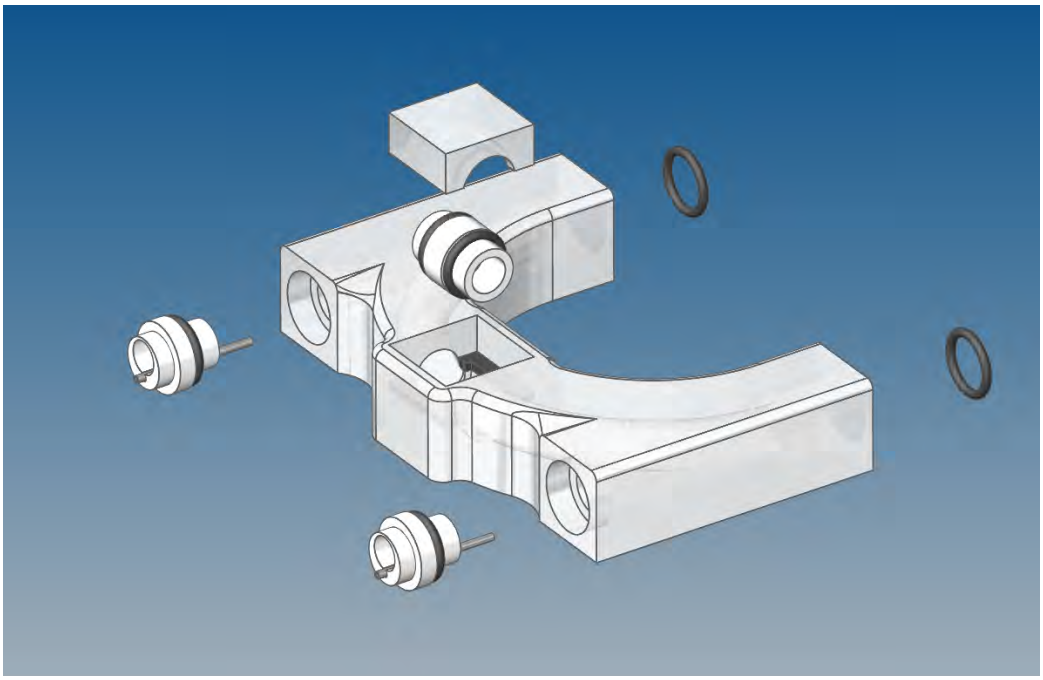

Figure 72: Assembled LT Chamber Juntion

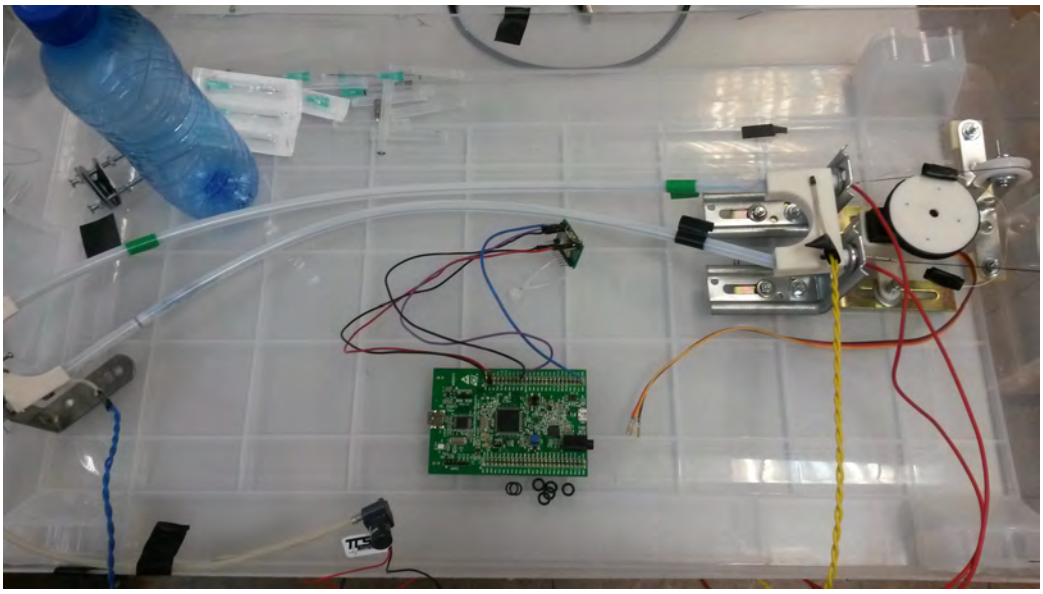

Figure 73: Preliminary Assembly

These pie charts indicate how much volume has been added to the bare SMA wire and shed light onto where more optimization needs to happen. Outer tubing alternatives are already under development, hopefully also reducing on the fluid share; pump may be shared between multiple actuators, reducing its proportional weight per actuator; servo gearing can be purposely designed,

and its package included on 3D printed parts. We would like to set SMA wire percentage at 25% to keep an interesting power-to-weight ratio.

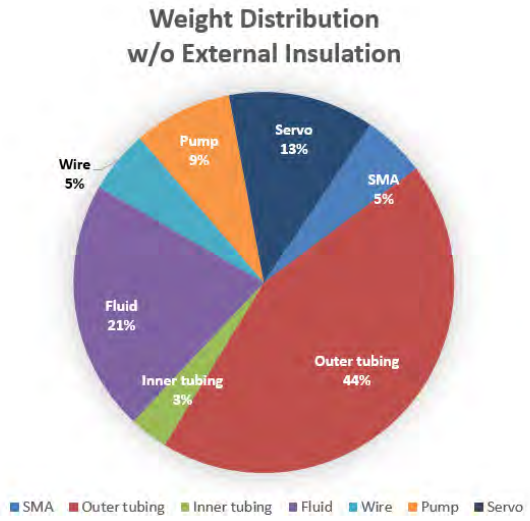

Figure 74: Weight Distribution

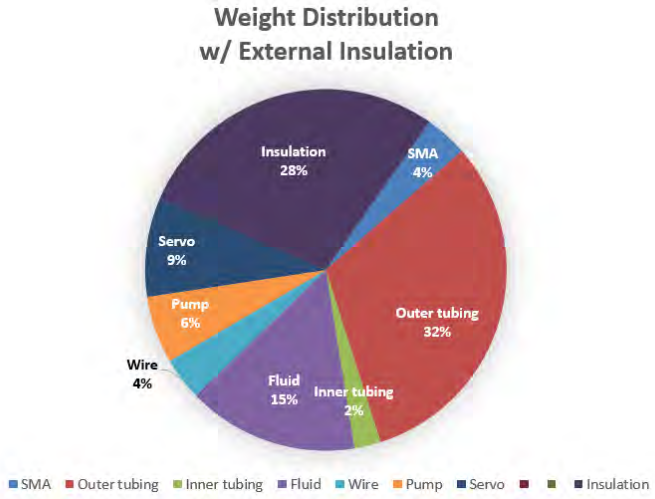

Figure 75: Weight Distribution

8 Conclusions

Given the forecoming situation presented on the introduction, we need a lot of breakthrough research taking place in these areas in the years to come.

The proposed actuator topology tries to put SMA-based actuators energy efficiency as close as possible to its theoretical limit while improving its actuation time. Further research is required for finding this new SMA-based actuator topology potential, which hopefully will take place along the next year. In any case, results look promising.

9 Appendix A: Engineering Drawings

REVISION HISTORY			
REV	DESCRIPTION	DATE	APPROVED

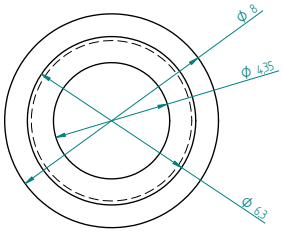

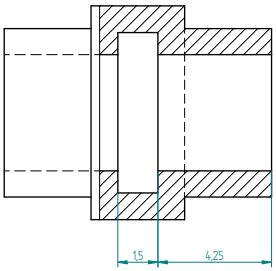

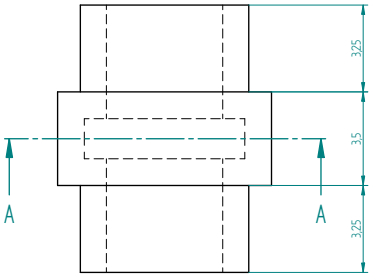

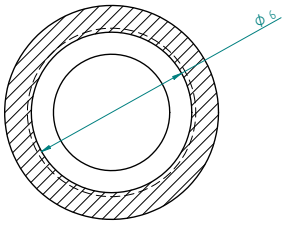

SECTION A–A

	NAME	DATE
DRAWN	room	04/19/16
CHECKED		
ENG APPR.		
MGR APPR.		

UNLESS OTHERWISE SPECIFIED
DIMENSIONS ARE IN MILLIMETERS
ANGLES ±X.X°
2 PL ±X.XX 3 PL ±X.XXX

Solid Edge

TITLE

SIZE	DWG NO	REV
A2		

FILE NAME: JDTrev3.dft

SCALE:	WEIGHT:	SHEET 1 OF 1

REVISION HISTORY			
REV	DESCRIPTION	DATE	APPROVED

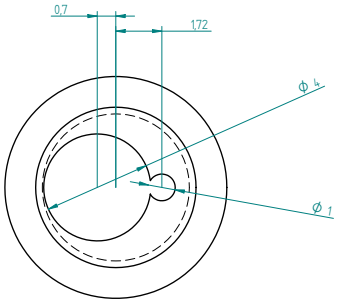

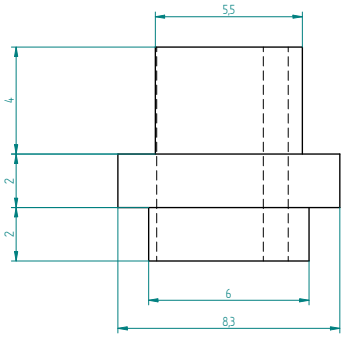

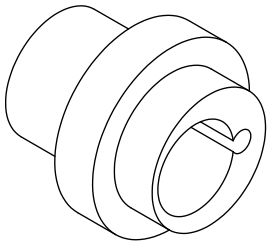

	NAME	DATE
DRAWN	room	06/02/16
CHECKED		
ENG APPR.		
MGR APPR.		

UNLESS OTHERWISE SPECIFIED
DIMENSIONS ARE IN MILLIMETERS
ANGLES ±X.X°
2 PL ±X.XX 3 PL ±X.XXX

Solid Edge

TITLE

SIZE	DWG NO	REV
A2		

FILE NAME: EXCr2.dft

SCALE:	WEIGHT:	SHEET 1 OF 1

REVISION HISTORY			
REV	DESCRIPTION	DATE	APPROVED

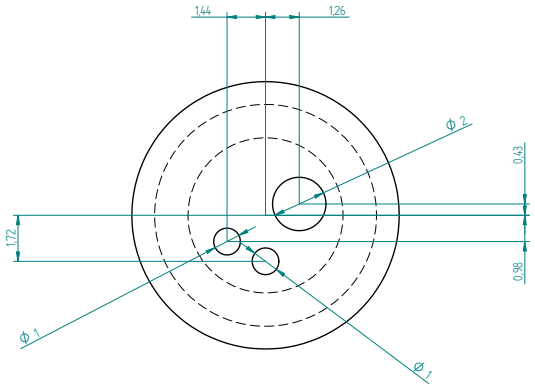

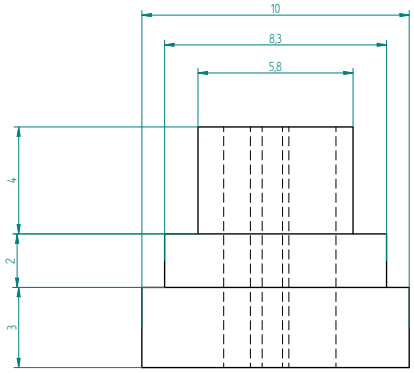

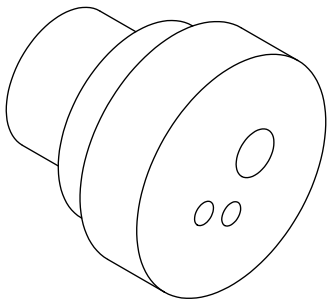

	NAME	DATE
DRAWN	room	06/02/16
CHECKED		
ENG APPR.		
MGR APPR.		

UNLESS OTHERWISE SPECIFIED
DIMENSIONS ARE IN MILLIMETERS
ANGLES ±X.X°
2 PL ±X.XX 3 PL ±X.XXX

Solid Edge

TITLE

SIZE	DWG NO	REV
A2		

FILE NAME: EXHr2.dft

SCALE:	WEIGHT:	SHEET 1 OF 1

REVISION HISTORY			
REV	DESCRIPTION	DATE	APPROVED

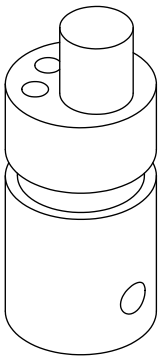

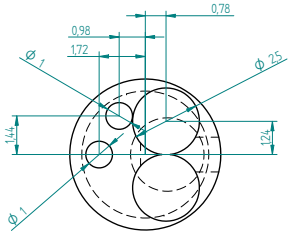

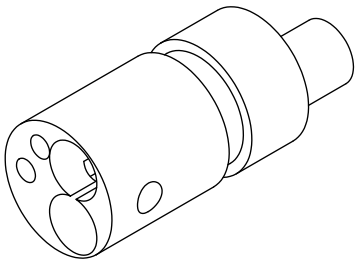

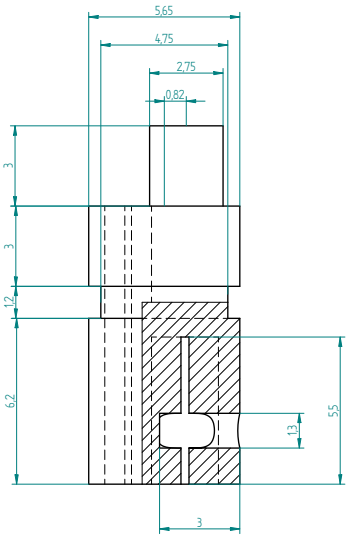

	NAME	DATE
DRAWN	room	06/02/16
CHECKED		
ENG APPR.		
MGR APPR.		

UNLESS OTHERWISE SPECIFIED
DIMENSIONS ARE IN MILLIMETERS
ANGLES ±X.X°
2 PL ±X.XX 3 PL ±X.XXX

Solid Edge

TITLE

SIZE	DWG NO	REV
A2		

FILE NAME: HCr7.dft

SCALE:	WEIGHT:	SHEET 1 OF 1

10 Appendix B: MATLAB Code

10.1 Pulley Diameter Visual Optimization

```
vl=0.10; %m/s
F=24; %N
maxspeed=150; %rpm
minspeed=40;
maxtorque=1.2; %Nm
mintorque=0.2;
mindiameter0.02; %m
maxdiameter=0.06;

vmax=linspace(minspeed,maxspeed,300);
D = linspace(mindiameter,maxdiameter,300);
[DG,vmaxG] = meshgrid(D,vmax);

Tmax=(F*(DG/2))./(1-(vl*60)./(pi*vmaxG.*DG));
Tmax(find(Tmax<0))=1.4;

figure('Position', [100, 100, 1500, 700],'Color',[1 1 1]);
subplot(1,3,1)
surf(DG,vmaxG,Tmax)
shading interp
view(0,0)
alpha('y')
alim([0 70])
axis([D(1) D(end) vmax(1) vmax(end) mintorque maxtorque -1 3])
subplot(1,3,2)
surf(DG,vmaxG,Tmax)
shading interp
view(90,0)
alpha('y')
alim([0 10])
axis([D(1) D(end) vmax(1) vmax(end) mintorque maxtorque -1 3])
subplot(1,3,3)
surf(DG,vmaxG,Tmax)
shading interp
view(0,90)
axis([D(1) D(end) vmax(1) vmax(end) mintorque maxtorque -1 3])
```

11 Appendix C: Budget

Item	Description	Unit	Quantity	Unit Price	Total Price
Inner tubing	Pneumatic Polyamide 2,7/4mm	m	2	0,50	1,00
Outer tubing	Pneumatic PTFE 6/8mm	m	2	5,44	10,88
Heating Element	AWG 40 Copper wire	m	5	0,33	1,65
Glue	Loctite 401 20g	u	1	19,00	19,00
O-rings	HNBR 70 4,7 x 0,7	u	2	0,05	0,10
	NBPR 70 4,0x1,0	u	1	0,17	0,17
	NBPR 70 6,0x1,0	u	10	0,17	1,70
Heat-transfer Fluid	Distilled Water Bottle	u	1	8,70	8,70
Pump	TCS M100S	u	1	59,49	59,49
Servo	Towerpro MG995	u	1	15,00	15,00
Motion wire	Monofilament PVDF	m	1	0,20	0,20
3D Printed Parts	Pulley, Servo Box, Junctions, Forming Mold	u	8	4,20	33,60
OT Machined Parts	Piston Skeleton, LT End, HT End, Sliding Flow Restrictor	u	5	14,00	70,00
PCB Fabrication	2-sided, Copper, Drilled	u	1	6,21	6,21
Electrical Components	Low Rd MOSFETs, Rail-to-rail amplifiers, Microthermistors	u	7	-	11,27
Needles	21 G Hypodermic	u	8	0,10	0,80
Grease	Rocol Aqua-Sil	u	1	22,29	22,29
STM32F4 Discovery	Dev Kit	u	1	10,19	10,19
Hardware	Framing Squares, Sliding Bolts, Long Bolts, Ball Bearing	u	20	-	13,11
Box	60x40, Reinforced Plastic	u	1	9,95	9,95
TOTAL					295,31

12 Appendix D: Gantt Chart

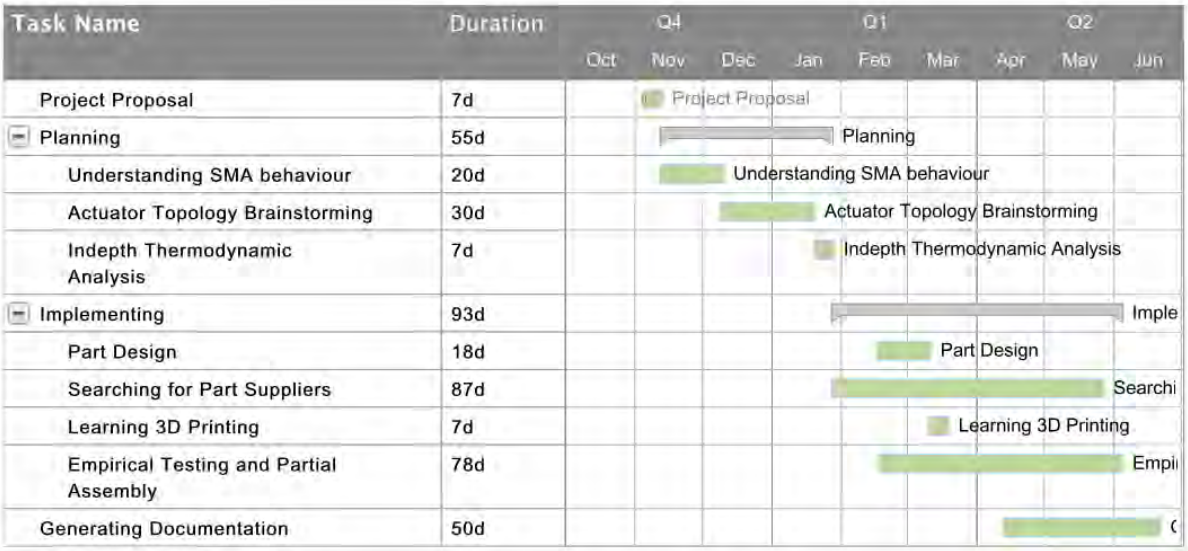

13 Glossary

ADC analog-to-digital converter
Advection transport mechanism of a substance or conserved property by a fluid due to the fluid's bulk motion.
cP (or cps) centipoise, unit for viscosity
DAC digital-to-analog converter
DoF degrees of freedom
DSC differential scanning calorimetry
HT higher temperature
ID inner diameter
LT lower temperature
OD outer diameter
PA polyamide, nylon
PET polyethylene terephthalate
PTFE polytetrafluoroethylene
PVDF polyvinylidene fluoride
PWM pulse-width modulation
rpm revolutions per minute
SMA(s) shape memory alloy(s), metallic compound
SMP(s) shape memory polymer(s), thermoplastic compound
VHC volumetric heat capacity

References

[1] Charles Xie, Interactive Heat Transfer Simulations for Everyone, The Physics Teacher, Volume 50, Issue 4, pg. 237-240, 2012.

[2] UN World Population Prospects. *http://esa.un.org/unpd/wpp/*, 2008.

[3] Giulio Sabbati. Ageing population: projections 2010 - 2060 for the EU27. *http://www.europarl.europa.eu/eplibrary/LSS-Ageing-population.pdf*, December 2013

[4] Japan Statistics Bureau, Japan MIC, Japan Ministry of Health, Labour and Welfare *http://www.mhlw.go.jp/english/database/db-hw/*, 2005

[5] Gang Song, Shuxiang Guo.
Development of an Active Self-assisted Rehabilitation Simulator for Upper Limbs, 2006

[6] Miriam C. Reyes-Fernández et al.
An elecroestimulation system synchronized with movement for active rehabilitation , 2015

[7] M. G. van Elk et al.
A motorized gravity compensation mechanism used for active rehabilitation of upper limbs , 2005

[8] Marian Schoone, Peter van Os, Antonet Campagne. Robot-mediated Active Rehabilitation (ACRE) A user trial , 2007

[9] Kseniya Charova and Cameron Schaeffer and Lucas Garron. Computers and Robots: Decision-Makers in an Automated World. *https://cs.stanford.edu/people/eroberts/cs201/projects/2010-11/ComputersMakingDecisions/index.html*, March 2011

[10] K.M. Armattoe et al.
Modeling of latent heat effects on phase transformation in shape memory alloy thin structures, 2016

[11] E. Rocon, J.C. Moreno, J.A. Gallego and J.L. Pons. Wearable Robots in Rehabilitation Engineering Tremor Suppression, Rehabilitation Engineering, Tan Yen Kheng (Ed.), ISBN: 978-953-307-023-0, *http://www.intechopen.com/books/rehabilitation-engineering/wearable-robots-in-rehabilitation-engineering-tremor-suppression*, 2009

[12] Nick Parrotta, Nicholas McGill, Elizabth Beattie and Nikolay Vladimirov
Titan Arm *http://titanarm.com/* , 2013

[13] Yoshiyuki Sankai
HAL: Hybrid Assistive Limb based on Cybernics
http://sanlab.kz.tsukuba.ac.jp/sonota/ISSR_Sankai.pdf , 2011

[14] Carlos Gonzalez
What's the Difference Between Pneumatic, Hydraulic, and Electrical Actuators? *http://machinedesign.com/linear-motion/what-s-difference-between-pneumatic-hydraulic-and-electrical-actuators*, 2015

[15] John P. Whitney et al.
A Hybrid Hydrostatic Transmission and Human – Safe Haptic Telepresence Robot, 2016

[16] Tim Swift
OtherLab Orthotics, 2015

[17] Ekso Bionics selected by Boston Dynamics to execute Darpa Project
http://ir.eksobionics.com/press-releases/detail/334/eksotm-bionics-selected-by-googles-boston-dynamics-to , 2014

[18] Boston Dynamics' Marc Raibert on Next-Gen ATLAS: "A Huge Amount of Work"
http://spectrum.ieee.org/automaton/robotics/humanoids/boston-dynamics-marc-raibert-on-nextgen-atlas , 2016

[19] A. Villoslada, A. Flores, D. Copaci, D. Blanco, L. Moreno High-displacement Flexible Shape Memory Alloy actuator for soft wearable robots, 2015

[20] W. T. Dempster.
Space Requirement of the Seated Operator - p. 187, 1955

[21] C. Liang and C. Roger.
One-dimensional thermomechanical constitutive relations for shape memory materials , 1990

[22] Viscosity. Experimental data from The Dortmund Data Bank.
https://en.wikipedia.org/wiki/Viscosity

[23] ISO-VG viscosities grades for industrial lubricants
http://www.engineeringtoolbox.com/iso-vg-grade-d_1206.html

[24] M. Vera, I. Iglesias, A. L. Sánche, C. Martínez
Ingeniería Fluidomecánica, pg. 175

[25] Tristen Hohman
Exploring the Motions of Long Bubbles in Tubes , 2010

[26] Apple Rubber Products
Seal Design Guide *http://www.applerubber.com/src/pdf/seal-design-guide.pdf*

[27] Needle gauge comparison chart *https://en.wikipedia.org/wiki/Needle_gauge_comparison_ch*

[28] Piaras Kelly Solid Mechanics Part I: An Introduction to Solid Mechanics, pg. 244-245

[29] Professional Plastics *http://www.professionalplastics.com/professionalplastics/MechanicalPr*

[30] Bikramjit Singh
Machine Design. Delhi University. *http://ecoursesonline.iasri.res.in/mod/page/view.php?id=*

[31] TohoTenax Datasheet *http://www.swiss-composite.ch/pdf/t-Tenax-Datenblatt.pdf*

[32] Steve Gerbig
Polyamide Moisture Absorption: Relative Dimensional Change of Various Nylon Products *http://knowledge.ulprospector.com/1390/polyamide-moisture-absorption/*, 2014

[33] Quadrant Manufactured PVDF Datasheet *http://www.quadrantplastics.com/fileadmin/quadrant/documents/QEPP/EU/Product_Data*

[34] Pololu DC Motors FAQ *https://www.pololu.com/product/1117/faqs*

[35] Art Fortini
Lightweight, Low-Cost Heatsink for High-Heat Flux ,2006

[36] K. Boomsma, D. Poulikakos, F. Zwick. Metal foams as compact high performance heat exchangers, 2003

[37] Ming H. Wu and L. McD. Schetky
Industrial Applications for Shape Memory Alloys. *http://www.memry.com/sites/default/files/documents /Nitinol_Industrial_Applications_SMST00.pdf*

[38] Teflon PTFE Properties Handbook by Dupont

[39] Clemens J. M. Lasance.
The Thermal Conductivity of Air at Reduced Pressures and Length Scales. *https://cs.stanford.edu/people/eroberts/cs201/projects/2010-11/ComputersMakingDecisions/index.html*, November 2002

[40] Epcos
NTC thermistors for temperature measurement, 2006